J. Fluid Mech. (1998), *vol.* 366, *pp.* 1–31. Printed in the United Kingdom

Local energy flux and subgrid-scale statistics in three-dimensional turbulence

By VADIM BORUE AND STEVEN A. ORSZAG†

Fluid Dynamics Research Center, Princeton University, Princeton, NJ 08544-0710, USA

(Received 13 November 1996 and in revised form 12 November 1997)

Statistical properties of the subgrid-scale stress tensor, the local energy flux and filtered velocity gradients are analysed in numerical simulations of forced three-dimensional homogeneous turbulence. High Reynolds numbers are achieved by using hyperviscous dissipation. It is found that in the inertial range the subgrid-scale stress tensor and the local energy flux allow simple parametrization based on a tensor eddy viscosity. This parametrization underlines the role that negative skewness of filtered velocity gradients plays in the local energy transfer. It is found that the local energy flux only weakly correlates with the locally averaged energy dissipation rate. This fact reflects basic difficulties of large-eddy simulations of turbulence, namely the possibility of predicting the locally averaged energy dissipation rate through inertial-range quantities such as the local energy flux is limited. Statistical properties of subgrid-scale velocity gradients are systematically studied in an attempt to reveal the mechanism of local energy transfer.

1. Introduction

Perhaps the most important feature of three-dimensional turbulence is the energy flux from large to small scales where energy is dissipated via viscous effects. In the limit as the viscosity goes to zero, the total amount of energy dissipation has according to Kolmogorov's (1941) theory a finite non-zero limit. The mechanism of dissipation in this zero-viscosity limit is purely dynamical. The singularity of the zero-viscosity limit reveals itself in the fact that although viscosity is an irrelevant parameter in the inertial range, it eventually provides dissipation at the smallest scales of the system. In other words, viscosity provides an ultraviolet cutoff at a dissipation wavenumber k_d. In the inertial range, the fluid is effectively described by the inviscid equations while the direction of the energy flux imposes irreversibility on the flow. Revealing the dynamics of this local energy flux is one of the most fundamental problems in turbulence. It is also of practical importance for the large-eddy simulation (LES) of turbulent flows.

We use filtering to give an intuitive idea of scales of motion (see for example Germano 1992). For a low-pass spatial isotropic filter of scale ℓ the filtered large-scale velocity is

$$\langle v_i \rangle_\ell = \int \varphi_\ell(x-y) v_i(y) \mathrm{d}^3 y. \tag{1.1}$$

For scales ℓ for which the molecular viscosity term is negligible the filtered Navier–

† Present address: Department of Mathematics, Yale University, New Haven, CT 06520-8283, USA.

Stokes equation for an incompressible turbulent flow takes the form

$$\frac{\mathrm{D}_\ell \langle v_i\rangle_\ell}{\mathrm{d}t} \equiv \frac{\partial \langle v_i\rangle_\ell}{\partial t} + \langle v_j\rangle_\ell \frac{\partial \langle v_i\rangle_\ell}{\partial x_j} = -\frac{\partial}{\partial x_j}\left(\langle p\rangle_\ell \delta_{ij} + \tau_{ij}\right) \tag{1.2}$$

with pressure $\langle p\rangle_\ell$ determined from $\partial_i \langle v_i\rangle_\ell = 0$ and subgrid-scale (SGS) stress tensor

$$\tau_{ij} = \langle v_i v_j\rangle_\ell - \langle v_i\rangle_\ell \langle v_j\rangle_\ell . \tag{1.3}$$

At inertial-range scales, the molecular viscosity term is irrelevant and is dropped in (1.2). Summation over repeated indexes is implied throughout if not stated otherwise.

The large-scale energy balance is deduced from (1.2) in the form

$$\partial_t E_\ell + \nabla \cdot \boldsymbol{J}_\ell = -\boldsymbol{\Pi}_\ell . \tag{1.4}$$

Here $E_\ell = \langle \boldsymbol{v}\rangle_\ell^2/2$,

$$\boldsymbol{J}_\ell = \left(\langle p\rangle_\ell + E_\ell\right)\langle \boldsymbol{v}\rangle_\ell + \tau \cdot \langle \boldsymbol{v}\rangle_\ell \tag{1.5}$$

and

$$\boldsymbol{\Pi}_\ell = -\partial_i \langle v_j\rangle_\ell \tau_{ij}. \tag{1.6}$$

The term $\boldsymbol{J}_\ell$ in (1.4) represents the convective contribution to the energy flux at inertial-range scales while the term $\boldsymbol{\Pi}_\ell$ represents the local energy flux from large scales to small scales (see Eyink 1995). $\boldsymbol{\Pi}_\ell$ gives the 'effective dissipation' of energy at scales larger than ℓ due to the action of scales smaller than ℓ on the gradient of the large-scale motion. For stationary homogeneous turbulence,

$$\langle \boldsymbol{\Pi}_\ell\rangle = \bar{\mathscr{E}}, \tag{1.7}$$

where $\bar{\mathscr{E}}$ is the average energy dissipation rate.

Locality of energy transfer holds if $\boldsymbol{\Pi}_\ell$ depends only on local gradients of large-scale velocity. The standard way to model the SGS stresses is to introduce a scalar eddy viscosity v_ℓ defined by

$$\tau_{ij} = -v_\ell \langle S_{ij}\rangle_\ell , \tag{1.8}$$

where $S_{ij} = (\partial_i v_j + \partial_j v_i)/2$ is the strain rate. A popular model of v_ℓ is Smagorinsky's (1963) model

$$v_\ell = 2(c_s \ell)^2 \left(\langle S_{ij}\rangle_\ell \langle S_{ij}\rangle_\ell\right)^{1/2} . \tag{1.9}$$

The concept of scalar eddy viscosity plays a central role in most turbulence closures or renormalization group calculations. It is usually assumed that elimination of small-scale degrees of freedom leads to enhanced scalar eddy viscosity.

A number of attempts have been made recently to check the representation (1.8) in direct numerical simulations or laboratory experiments (see Liu, Meneveau & Katz 1994 for a review). This approach, frequently called *a priori* testing, was pioneered by Clark, Ferziger & Reynolds (1979). It consists of using fully resolved velocity fields to compare the local instantaneous subgrid stress with the prediction of the subgrid-scale model. With this approach it has been repeatedly observed that scalar eddy viscosity closures and the Smagorinsky model in particular display little correlation with the real stress τ_{ij}. On the other hand, it was noticed by Bardina, Ferziger & Reynolds (1980) that τ_{ij} at scale ℓ shows a high correlation with τ_{ij} at larger scales (say those between ℓ and 2ℓ). The assumption that τ_{ij} equals the resolved stresses at scales between ℓ and 2ℓ is called the scale-similarity model. Recently, similar results were obtained by Liu *et al.* (1994), where this representation was called the nonlinear model. Basically this model goes back to Leonard (1974) and in the simplest form

states that

$$\tau_{ij} = c_n \ell^2 \langle A_{ik} \rangle_\ell \langle A_{jk} \rangle_\ell , \tag{1.10}$$

where c_n is some $O(1)$ constant and

$$\langle A_{ij} \rangle_\ell = \frac{\partial \langle v_i \rangle_\ell}{\partial x_j}. \tag{1.11}$$

The representation (1.10) is essentially equivalent to the representation of τ_{ij} in the scale-similarity model of Bardina *et al.* (1980). As follows from (1.10) the eddy viscosity in this case is not a scalar but a tensor quantity. We will call such a model the tensor eddy viscosity representation.

Here we present an *a priori* numerical study of the statistical properties of the SGS stress tensor τ_{ij}. We present data demonstrating that the representation (1.10) accurately describes the statistics of τ_{ij}. However, we emphasize that a fundamental drawback of *a priori* analysis based on direct numerical simulations data is the restriction to relatively low Reynolds numbers.

In previous work (Borue & Orszag 1995*a*), we have already demonstrated that for given numerical resolution, we can effectively increase the extent of the inertial range of three-dimensional turbulence by an order of magnitude by using alternative forms of dissipation. To do this, we replace the normal Newtonian dissipation by a higher power of the Laplacian, i.e. hyperviscous dissipation. It was shown by Borue & Orszag (1995*a*, *b*, 1996*a*, *b*) that three-dimensional inertial-range dynamics is relatively independent of the form of the hyperviscosity and that modest resolution simulations with high-order hyperviscosity lead to sufficiently extensive inertial ranges that measurement of a broad variety of otherwise intractable flow quantities can be made. In this work we use the same numerical data set to analyse statistical properties of the subgrid-scale stress.

A scalar eddy viscosity representation of the SGS stress tensor will always lead to a positive local energy flux (see (1.7)) It is known from the LES literature (see Reynolds 1990 for a review) that in *a priori* tests the local energy flux defined by (1.6) is not positive. Such negative local energy flux is usually called 'backscatter' in the literature. In contrast with a scalar eddy viscosity, tensor viscosity can lead to a local energy flux that is not always positive. The tensor eddy viscosity representation (1.10) leads to an expression for the local energy flux that accurately describes both regions of positive local energy flux and the backscatter regions where the local energy flux is negative. The sign of the local energy flux depends on the local values of velocity gradients. Using (1.6) and (1.10), the local energy flux can be represented as

$$\boldsymbol{\Pi}_\ell = c_n \ell^2 [-\mathrm{Tr}\left(\langle \boldsymbol{S} \rangle_\ell^3\right) + \tfrac{1}{4} \langle \omega_i \rangle_\ell \langle S_{ij} \rangle_\ell \langle \omega_j \rangle_\ell], \tag{1.12}$$

where $\omega_i = \varepsilon_{ijk} \partial_j v_k$ is vorticity and the symbol Tr stands for the trace of a matrix. From (1.12), it follows that the local energy flux is positive if the skewness of the filtered strain matrix is negative and the vorticity production (stretching) term $\langle \omega_i \rangle_\ell \langle S_{ij} \rangle_\ell \langle \omega_j \rangle_\ell$ is positive. It has been known for a long time that, in turbulence, the average derivative skewness is negative and the stretching term is positive (see for example Orszag 1973 or Monin & Yaglom 1975). The symmetric matrix $\langle S_{ij} \rangle_\ell$ is characterized by its three real eigenvalues $z_{1,2,3}$, whose sum must be zero by incompressibility. One of these eigenvalues is always positive, $z_1 > 0$, another is always negative, $z_3 < 0$. The sign of $\mathrm{Tr}(\langle S \rangle_\ell^3) = 3 z_1 z_2 z_3$ depends on the sign and the probability distribution of the middle eigenvalue z_2. If the middle eigenvalue z_2 is predominately positive when z_1 is large the strain matrix is negatively skewed.

Note that in the case of inviscid dynamics the tensor eddy viscosity model (1.10) leads to effective equations that are time-reversal invariant. This is in contrast with the scalar eddy viscosity representation (1.8). However, constraining the local energy flux (1.12) or the skewness to be non-zero breaks the time reversibility of the Euler equations. The possible dynamical mechanism involved in this behaviour was suggested by Viellefosse (1982, 1984), who showed that, in the local interaction approximation, Eulerian dynamics leads to a singularity in finite time. At times near the singularity, there is a strongly negative derivative skewness $z_2 > 0$ in which also vorticity is aligned with the middle eigenvector leading to positivity of the stretching term. An exact solution of Viellefosse's equations was obtained recently by Cantwell (1992). As might be expected non-locality and viscosity smooth out the singularity. However, what is important is the basic instability of local velocity gradient dynamics that produces the positive local energy flux. (The issue of finite time singularities of three-dimensional Eulerian dynamics remains open, although recent evidence tends to support their existence (R. Pelz 1996, R. Kerr 1996, personal communications)).

In this work we systematically study the dynamics of velocity gradients as a function of scale. Early work on this was done by Ashurst *et al.* (1987) who demonstrated that the geometry of small-scale motion in isotropic turbulence exhibits a number of features in common with the results of Viellefosse. Since then a number of similar results were obtained by other groups (see Cantwell 1993 and She, Jackson & Orszag 1991 for reviews). In this work we partially repeat some of the measurements done before while adding new results.

2. Technical background

2.1. *Numerical methods*

We solve the hyperviscosity modified Navier–Stokes equations in a periodic three-dimensional cube of sides $L = 2\pi$ with large-scale isotropic white-in-time forcing using numerical resolutions N^3, $N = 64, 128, 256$. The hyperviscosity-modified Navier–Stokes equations are

$$\partial_t v_i + v_j \partial_j v_i = -\partial_i p + (-1)^{h+1} \nu_h \Delta^h v_i + f_i, \tag{2.1}$$

where the pressure p is calculated from the incompressibility condition $\partial_i v_i = 0$. On the right-hand side of (2.1) we include a force which is non-zero only at some characteristic scale k_f

$$\langle f_i(\boldsymbol{k}, t) f_j(\boldsymbol{k}', t') \rangle \sim \delta_{ij} \delta(k^2 - k_f^2) \delta(\boldsymbol{k} + \boldsymbol{k}') \delta(t - t'), \tag{2.2}$$

and a hyperviscous dissipation designed to provide an energy sink at small scales. The Gaussian force f is chosen to act only on the smallest wavenumber shells $k_f = 1, 2$. The power $h = 8$ of the hyperviscous dissipation is chosen to maximize the extent of the inertial range (see Borue & Orszag 1996*a*). The hyperviscosity coefficient ν_h with $h = 8$ is chosen so that $\nu_h (N/2)^{2h} \delta t \approx 0.5$, where δt is the time step of the numerical scheme. The time step on the other hand is fixed by the characteristic maximum velocity at large scales v_{max} according to the Courant number criterion: $v_{max} \delta t N / 2\pi \leqslant 0.2$. The characteristic velocity is set by specifying the amplitude of the force (2.2). The Reynolds number in this setting is independent of the amplitude of the force. Thus all parameters of (2.1) are uniquely defined by the large-scale flow and the numerical resolution. We solve (2.1) using a parallel pseudospectral code described by Jackson, She & Orszag (1991).

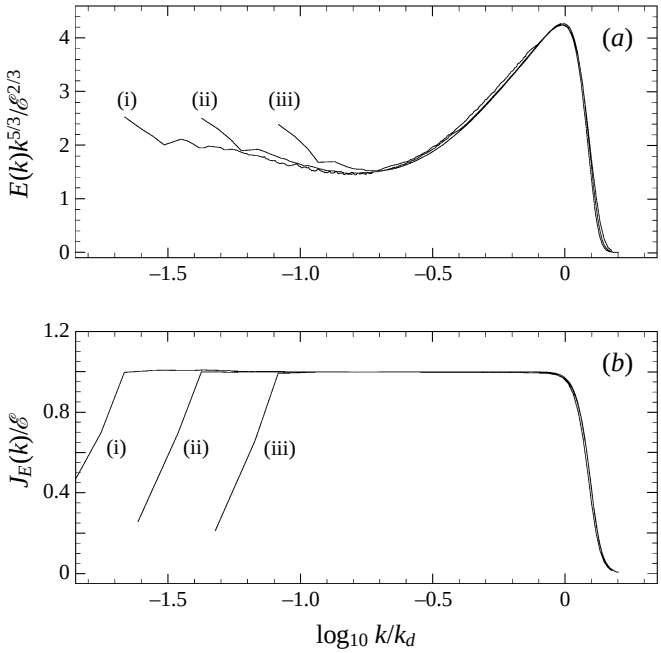

FIGURE 1. (*a*) Scaled energy spectra $E(k)k^{5/3}/\bar{\mathscr{E}}^{2/3}$ (part of the spectra corresponding to $k = 1, 2$ are not shown) and (*b*) scaled energy fluxes $J_E(k)/\bar{\mathscr{E}}$ as functions of $\log_{10}k/k_d$. Resolutions 256^3 (i), $k_d = 82$; 128^3 (ii), $k_d = 41$ and 64^3 (iii), $k_d = 21$. Hyperviscosity with $h = 8$ is used.

In a statistically steady state, a constant energy flux

$$J_E(k) = \int_{k'>k}^{\infty} T(k')\mathrm{d}k' \tag{2.3}$$

has been observed (Borue & Orszag 1995*a*) for $k_f \leqslant k \leqslant k_d$. Here $T(k)$ is the energy transfer function and k_d is defined as the wavenumber at which the maximum of the vorticity spectrum $k^2E(k)$ is attained ($k_d \approx N/3$ for $h = 8$ where we assume henceforth that wavenumbers are measured in $2\pi/L = 1$ units). The definition of the k_d through the vorticity spectrum leads to the approximate independence of k_d of the hyperviscosity type h. The isotropic energy spectrum $E(k)$ is expected (Kolmogorov 1941) to have the form:

$$E(k) = 2\pi k^2 \langle v_i(-\boldsymbol{k})v_i(\boldsymbol{k})\rangle = \frac{\bar{\mathscr{E}}^{2/3}}{k^{5/3}} G(k/k_d, k_d/k_f) \tag{2.4}$$

with possible anomalous dimensions (deviations from Kolmogorov scaling) included in the function G. Here $\bar{\mathscr{E}}$ is the mean energy dissipation rate set by the external forcing. In the case of hyperviscous dissipation the energy dissipation rate is defined as

$$\mathscr{E} = \nu_h \Delta^{h/2} v_i \Delta^{h/2} v_i. \tag{2.5}$$

The Taylor-microscale Reynolds number for hyperviscous turbulence is defined as (Borue & Orszag 1995*a*)

$$R_\lambda \approx 50 \left(\frac{k_d}{k_f}\right)^{2/3}. \tag{2.6}$$

The various characteristics of the statistically steady state in this case are described

in Borue & Orszag (1995 *a*, 1996 *b*). Some deviations of the energy spectrum $E(k)$ observed in Borue & Orszag (1995 *a*) are linked to persistent large-scale anisotropy in Borue & Orszag (1995 *b*). For decaying turbulence, Kolmogorov's 5/3 law is recovered (Borue & Orszag 1995 *b*). Regardless of the small deviations in the energy spectrum this numerical set-up is capable of correctly reproducing such subtle characteristics as the statistics of the energy dissipation rate (Borue & Orszag 1995 *b*).

In this work we consider the case of large-scale white-in-time Gaussian forcing (Borue & Orszag 1995 *a*, 1996 *b*). For completeness the isotropic energy spectra $E(k)$ and the energy fluxes $J_E(k)$ are plotted in figure 1.

The measurements reported here are carried out to assure statistical convergence of the results. Numerical integrations are performed over at least 10 large-eddy turnover times for each measurement. Convergence is also checked for each data set. Most of the measurements are performed for numerical resolution 128^3. To study the Reynolds number dependence some measurements are also performed for 64^3 and 256^3 resolutions.

2.2. *Filtering procedure*

For a field A we define a low-pass spatial isotropic filter of scale ℓ as a convolution

$$\langle A(\boldsymbol{x})\rangle_\ell = \int \varphi_\ell(\boldsymbol{x}-\boldsymbol{y})A(\boldsymbol{y})\mathrm{d}^3y. \tag{2.7}$$

There is no filtering in time. The convolution (2.7) is carried out naturally in Fourier space as

$$\left\langle \hat{A}(\boldsymbol{k})\right\rangle_\ell = \hat{\varphi}_\ell(\boldsymbol{k})\hat{A}(\boldsymbol{k}) \tag{2.8}$$

where $\hat{\varphi}_\ell(\boldsymbol{k})$ and $\hat{A}(\boldsymbol{k})$ are Fourier transforms of the corresponding fields. The filter is normalized by

$$\hat{\varphi}_\ell(0) = \int \varphi_\ell(x)\mathrm{d}^3x = 1. \tag{2.9}$$

The filters that are employed are

$$\left.\begin{aligned}
&\text{top-hat:}\quad \varphi_\ell(\boldsymbol{x}) = \frac{6}{\pi\ell^3}\theta(\tfrac{1}{2}\ell - r), && \hat{\varphi}_\ell(\boldsymbol{k}) = \tfrac{3}{\xi^3}\left[\sin(\xi) - \xi\cos(\xi)\right];\\
&\text{Gaussian:}\ \varphi_\ell(\boldsymbol{x}) = \left(\frac{10}{\pi\ell^2}\right)^{3/2}\exp\left(-\frac{10r^2}{\ell^2}\right), && \hat{\varphi}_\ell(\boldsymbol{k}) = \exp\left(-\frac{\xi^2}{10}\right);\\
&\text{cut-off:}\quad \varphi_\ell(\boldsymbol{x}) = \frac{1}{2\pi^2r^3}\left[\sin(\eta) - \eta\cos(\eta)\right], && \hat{\varphi}_\ell(\boldsymbol{k}) = \theta\left(\frac{\pi}{\ell} - |\boldsymbol{k}|\right),
\end{aligned}\right\} \tag{2.10}$$

where $r = |\boldsymbol{x}|$, $\xi = \frac{1}{2}|\boldsymbol{k}|\ell$, $\eta = \pi r/\ell$ and $\theta(x)$ is the θ-function.

All three filters are isotropic. The top-hat and Gaussian filters are positive in physical space, i.e. $\varphi_\ell(\boldsymbol{x}) \geqslant 0$. The cut-off filter is oscillatory. For the top-hat filter the moment of inertia is $\left\langle \boldsymbol{x}^2\right\rangle_\ell = 3\ell^2/20$ and the Gaussian filter is scaled so that it has the same moment $\left\langle \boldsymbol{x}^2\right\rangle_\ell$ as the top-hat filter. The cut-off filter is slowly decaying in space; the moment $\left\langle \boldsymbol{x}^2\right\rangle_\ell$ diverges. As can be seen only the Gaussian filter is non-oscillatory in both physical and Fourier space. The top-hat filter is oscillatory in wavenumber space. The cut-off and top-hat filters are extreme representations of so-called Butterworth-type filters. These can be made either non-oscillatory in physical space (positive) or in wavenumber space.

It turns out that if the filter is positive in physical space, the results discussed in this paper are practically independent of the type of filter. However, in some cases our results may be somewhat dependent on whether the filter is positive or oscillatory in physical space. While discussing the results, we will point out specifically if such a dependence has been observed. Moreover, the cut-off filter leads to similar results to Butterworth-type filters which are smooth in Fourier space but still oscillatory in physical space. Therefore, top-hat, Gaussian and cut-off filters serve as characteristic representatives of the various positive and oscillatory low-pass filters.

Since we believe that most of the physical quantities under study are local in space we prefer to use filters that are localized and positive in space, i.e. top-hat and Gaussian filters. This assures that if we filter a positive quantity, it will remain positive after filtering. Detailed discussion of issues of filter positivity can be found in Vreman, Geurts & Kuerten (1994) (see also Eyink 1996).

It is convenient to introduce the characteristic wavenumber of the filter

$$k_c = \frac{\pi}{\ell}. \tag{2.11}$$

To assure that filtered results are relatively independent of the dissipation range we chose k_c in the inertial range. Usually we carry out measurements for $k_c = 4, 8, ...N/4$. As can be seen from figure 1(*b*), these wavenumbers are within the range of the constant energy flux.

2.3. *Analysis of correlations*

As the basic tool in our analysis of correlations of various scalar, vector and tensor fields we use joint probability distributions of these fields. Each field is obtained simultaneously by the appropriate filtering procedure with the filtering performed in Fourier space. For example let us consider two such fields $A(\boldsymbol{x})$ and $B(\boldsymbol{x})$. In the case of isotropic, homogeneous and statistically stationary turbulence, the joint probability distribution $\mathscr{P}(A, B)$ can be calculated using a scatter plot of A, B with averaging performed both in space and in time.

The correlation coefficient between A and B is defined as

$$\rho(A, B) = \frac{\langle AB\rangle - \langle A\rangle \langle B\rangle}{\left[(\langle A^2\rangle - \langle A\rangle^2)(\langle B^2\rangle - \langle B\rangle^2)\right]^{1/2}} \tag{2.12}$$

where we indicate space–time averaging by $\langle ...\rangle$. We expect that if the variable A is nearly statistically equivalent to the variable B then the correlation coefficient $\rho(A, B)$ should be close to unity.

Another useful diagnostic is the average of one variable conditioned on another. For example the conditional average of B on A is defined as

$$\langle B|A\rangle = \frac{\int \mathrm{d}B B\mathscr{P}(A, B)}{\int \mathrm{d}B \mathscr{P}(A, B)} \tag{2.13}$$

For strongly correlated variables we expect that

$$A \approx \langle A|(\langle B|A\rangle)\rangle \quad \text{and} \quad B \approx \langle B|(\langle A|B\rangle)\rangle\,. \tag{2.14}$$

The joint probability distribution $\mathscr{P}(A, B)$ is visualized by plotting isocontours of $\log_{10}\mathscr{P}(A, B)$ in the (A, B)-plane. In addition we also plot $\langle A|B\rangle$ as well as $\langle B|A\rangle$.

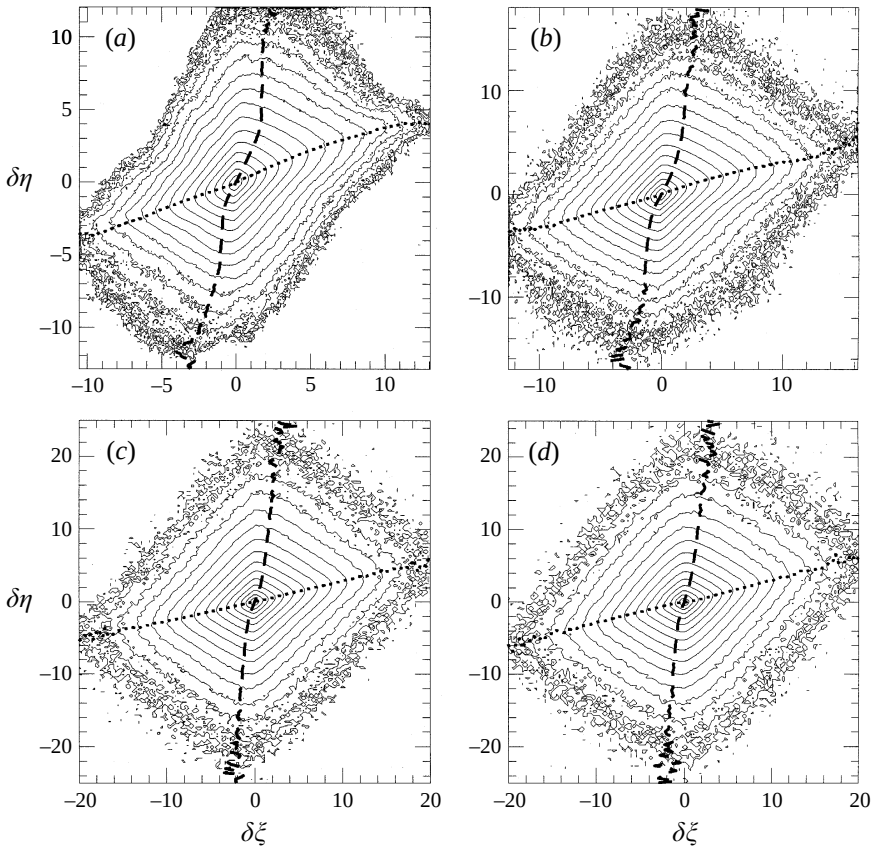

FIGURE 2. Joint PDFs between the Smagorinsky eddy viscosity tensor for its $i \neq j$ components $\xi = \mathscr{T}_{ij}^{(S)}$ and the same components of the actual SGS tensor $\eta = \tau_{ij}$. Top-hat filters are used. Means are subtracted and variables are normalized by their variances. The coefficient ρ is the correlation coefficient between these two tensors. Isocontours of $\log_{10} \mathscr{P}$ are plotted in increments of 0.4. Dotted curves are conditional averages of abscissas conditioned on ordinates and dashed curves are vice versa. The results are plotted for 128^3 numerical resolution ($k_d = 41$) and (*a*) $k_c = 4$, $\rho = 0.42$; (*b*) $k_c = 8$, $\rho = 0.37$; (*c*) $k_c = 16$, $\rho = 0.27$; (*d*) $k_c = 32$, $\rho = 0.23$.

3. Structure of the subgrid-scale stress tensor

In this section we present results on component-by-component correlation between the subgrid-scale tensor (1.3) directly measured in our simulations and the Smagorinsky eddy viscosity model (1.8) as well as the tensor eddy viscosity model (1.10).

3.1. *Scalar eddy viscosity*

With the scalar eddy viscosity model, the SGS stress tensor τ_{ij} is represented as

$$\mathscr{T}_{ij}^{(S)} = -2(c_s \ell)^2 \left(\langle \boldsymbol{S} \rangle_\ell^2 \right)^{1/2} \langle S_{ij} \rangle_\ell . \tag{3.1}$$

In our numerical simulation we simultaneously measure the SGS stress tensor $\tau_{ij}(\boldsymbol{x})$ and the Smagorinsky representation of this tensor $\mathscr{T}_{ij}^{(S)}(\boldsymbol{x})$ given by (3.1). The joint probability distribution $\mathscr{P}(\tau_{ij}, \mathscr{T}_{ij}^{(S)})$ for $i \neq j$ is plotted in figure 2. A top-hat filter is used and the data are obtained for the case of 128^3 numerical resolution. The

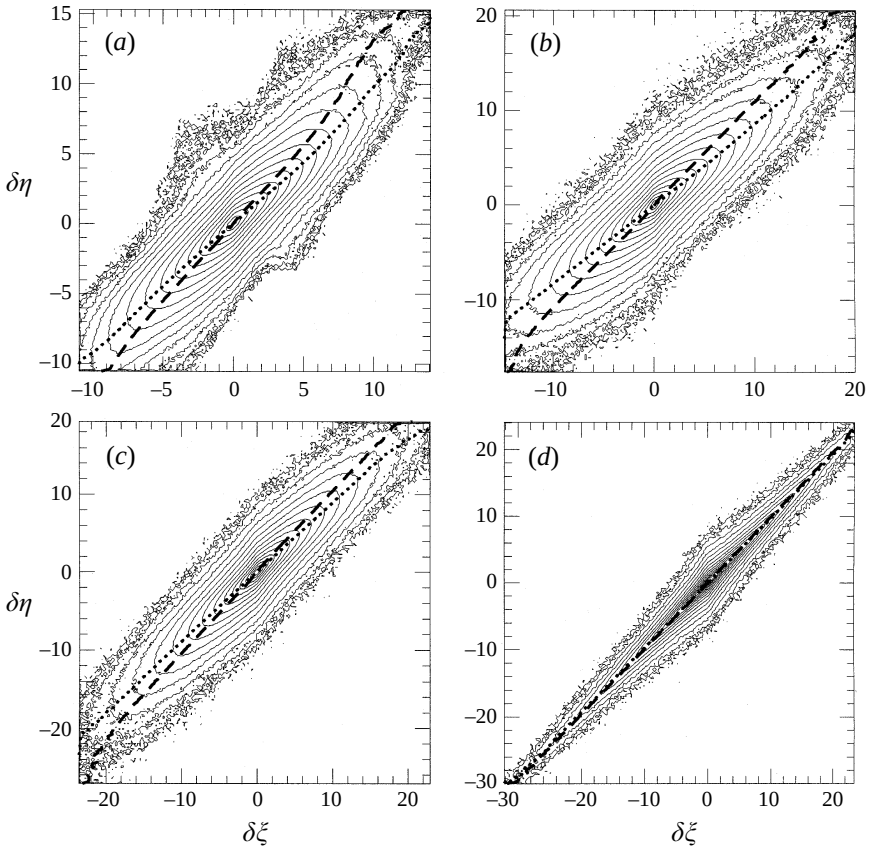

FIGURE 3. Joint PDFs between the tensor eddy viscosity representation for the $i \neq j$ components $\xi = \mathscr{T}_{ij}^{(T)}$ and the same components of the actual SGS tensor $\eta = \tau_{ij}$. Top-hat filters are used. For details see figure 2 caption. (*a*) $k_c = 4$, $\rho = 0.87$; (*b*) $k_c = 8$, $\rho = 0.83$; (*c*) $k_c = 16$, $\rho = 0.88$; (*d*) $k_c = 32$, $\rho = 0.97$.

correlation coefficient ρ between the actual SGS stress tensor and the scalar eddy viscosity representation decreases as the scale ℓ decreases. The correlation between τ_{ij} and $\mathscr{T}_{ij}^{(S)}$ is rather low (ρ changing from 0.42 for $k_c = 4$ to 0.23 for $k_c = 32$). These results are nearly independent of Reynolds number as checked using 256^3 numerical resolution. Moreover, the results remain unchanged when a Gaussian filter is used. However, the correlation decreases by nearly a factor of two when a cut-off filter is used. This observation is consistent with the results of Liu *et al.* (1994).

The observed correlation coefficient ρ is approximately twice as high as those that have been observed by Liu *et al.* (1994). We attribute the difference to the fact that we measured all components $i \neq j$ of both tensors. On the other hand, Liu *et al.* (1994) measured correlations between only a few components of the two tensors and the statistical data set in our case is substantially larger than theirs.

3.2. *Tensor eddy viscosity*

In this subsection we will demonstrate that a substantially higher level of correlations exists between the actual SGS stress tensor τ_{ij} and the tensor eddy viscosity

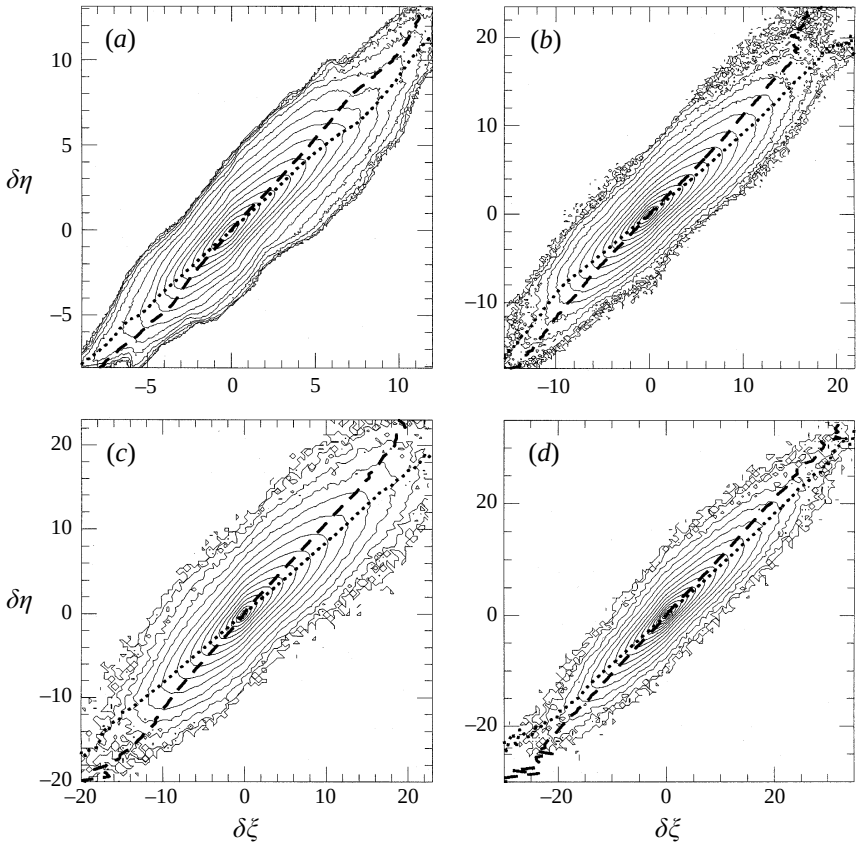

FIGURE 4. Joint PDFs between the diagonal components $i = j$ of the traceless tensor eddy viscosity representation $\xi = \mathscr{T}_{ij}^{(T)} - \frac{1}{3}\delta_{ij}\mathscr{T}_{\ell}^{(T)}$ and the same components of the traceless actual SGS tensor $\eta = \tau_{ij} - \frac{2}{3}\delta_{ij}\mathscr{K}_{\ell}$. Top-hat filters are used. For details see figure 2 caption. The results are plotted for 256^3 numerical resolution ($k_d = 82$) and (*a*) $k_c = 4$, $\rho = 0.9$; (*b*) $k_c = 8$, $\rho = 0.88$; (*c*) $k_c = 16$, $\rho = 0.83$; (*d*) $k_c = 32$, $\rho = 0.87$.

representation (see (1.10))

$$\mathscr{T}_{ij}^{(T)} = c_n \ell^2 \langle A_{ik} \rangle_{\ell} \langle A_{jk} \rangle_{\ell} . \tag{3.2}$$

As in the case of the scalar eddy viscosity representation, we measure the actual SGS stress tensor τ_{ij} and the tensor eddy viscosity representation $\mathscr{T}_{ij}^{(T)}$ for various filter sizes. The joint probability distribution obtained for the case of the top-hat filter $\mathscr{P}(\mathscr{T}_{ij}^{(T)}, \tau_{ij})$ is plotted in figure 3. The $i \neq j$ components of the tensors are used. As can be seen from figure 3, the correlation coefficient between the actual SGS stress tensor and the nonlinear representation of this tensor is high. Indeed, these two tensors are nearly identical.

The joint PDF plotted in figure 3 is obtained for 128^3 numerical resolution using the $i \neq j$ components of the tensors. We checked that the high level of correlations of these tensors remains the same in the case of higher Reynolds numbers (with 256^3 numerical resolution). The level of correlations between other components of these tensors is also high. To check the level of correlations of the diagonal components we need to check separately the correlations between traces of these tensors and correlations between their diagonal traceless parts. According to (1.3), the trace of

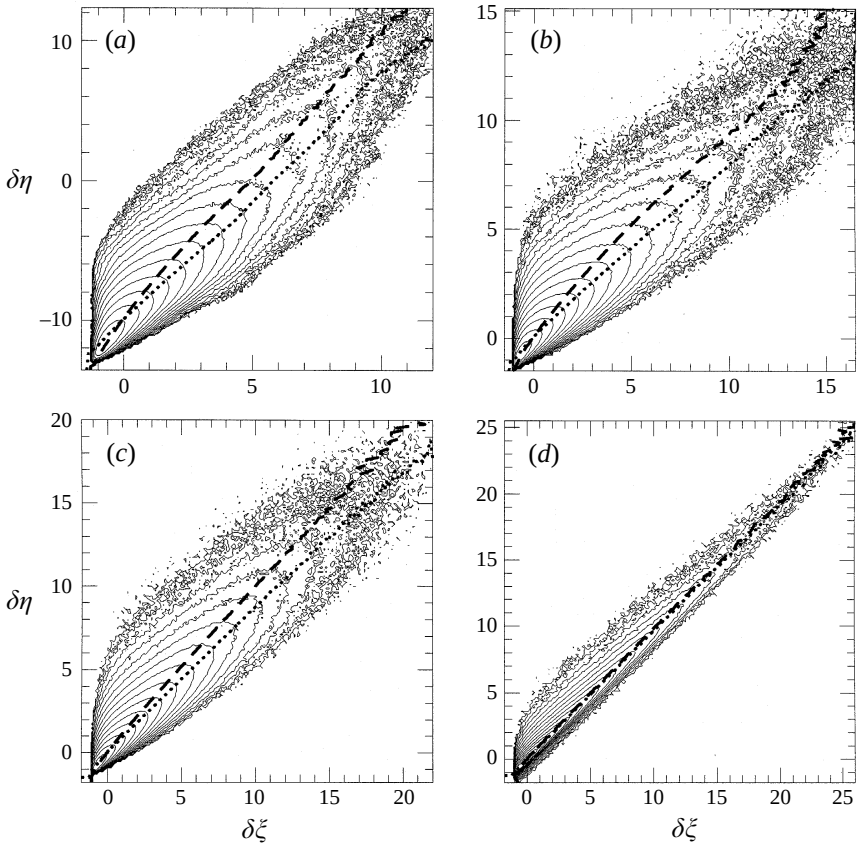

FIGURE 5. Joint PDFs between traces of the tensor eddy viscosity representation $\xi = \mathscr{T}_\ell^{(T)}$ and the actual SGS tensor $\eta = \mathscr{K}_\ell$. Top-hat filters are used. For details see figure 2 caption. The results are plotted for 128^3 numerical resolution and ($k_d = 41$) (*a*) $k_c = 4$, $\rho = 0.86$; (*b*) $k_c = 8$, $\rho = 0.87$; (*c*) $k_c = 16$, $\rho = 0.91$; (*d*) $k_c = 32$, $\rho = 0.97$.

the actual SGS tensor τ_{ij} is twice the SGS turbulent energy

$$\mathscr{K}_\ell = \tfrac{1}{2}\tau_{ii} = \tfrac{1}{2}\left(\langle v_i v_i\rangle_\ell - \langle v_i\rangle_\ell \langle v_i\rangle_\ell\right). \tag{3.3}$$

The trace of $\mathscr{T}_{ij}^{(T)}$ according to (1.10) and (1.11) is

$$\mathscr{T}_\ell^{(T)} = \mathscr{T}_{ii}^{(T)} = c_n \ell^2 \left(\langle \boldsymbol{S}\rangle_\ell^2 + \tfrac{1}{2}\langle\omega\rangle_\ell^2\right). \tag{3.4}$$

The joint PDF of the diagonal components of the traceless actual SGS tensor and the traceless tensor eddy viscosity representation $\mathscr{P}(\mathscr{T}_{ij}^{(T)} - \frac{1}{3}\delta_{ij}\mathscr{T}_\ell^{(T)}, \tau_{ij} - \frac{2}{3}\delta_{ij}\mathscr{K}_\ell)$ is plotted in figure 4. To illustrate the Reynolds number independence of the correlations we plot the joint PDF for the case of 256^3 numerical resolution. As can be seen from figure 4, a high level of correlation is also observed. The application of the smallest-scale filter with $k_c = 32$ for the case of 128^3 resolution leads to a correlation coefficient $\rho = 0.97$ (see figure 3*d*). For the same scale $k_c = 32$ the higher Reynolds number data leads to the correlation coefficient $\rho = 0.87$ (see figure 4*d*). Therefore, for the case of 128^3 resolution, the smallest-scale filter has a scale which is too close to the dissipation range. On the other hand, in the case of 256^3 numerical resolution,

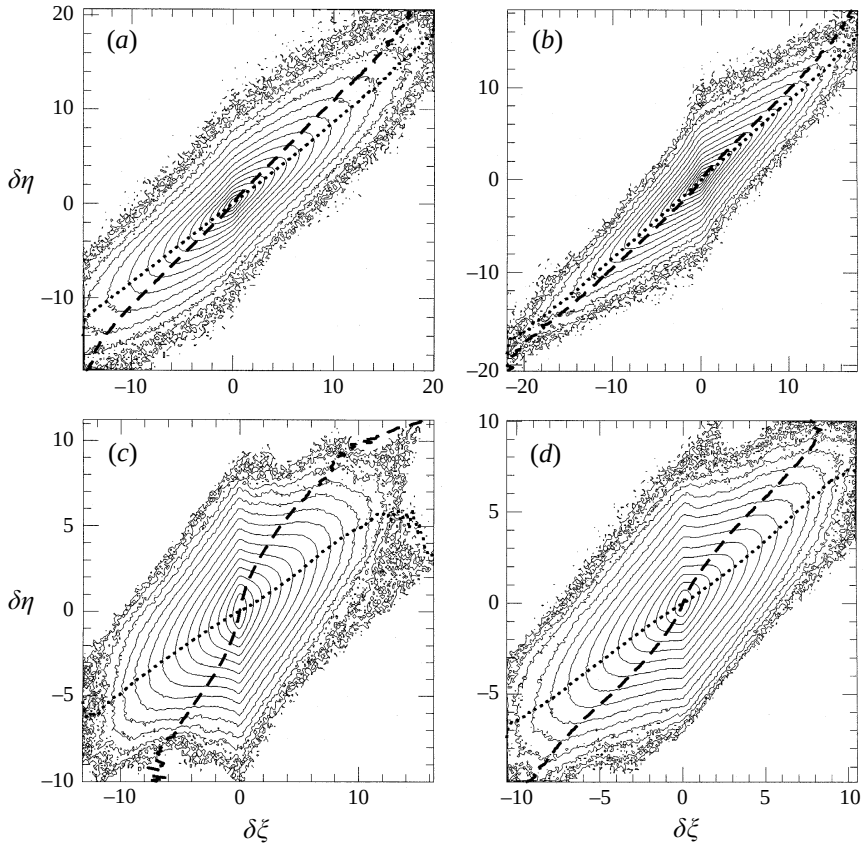

FIGURE 6. Joint PDFs between the $i \neq j$ components of the tensor eddy viscosity representation $\xi = \mathscr{T}_{ij}^{(T)}$ and the actual SGS tensor $\eta = \tau_{ij}$ for different filter types. For details see figure 2 caption. The results are plotted for 128^3 numerical resolution ($k_d = 41$) and filter scale $k_c = 8$ for (*a*) top-hat filter, $\rho = 0.84$; (*b*) Gaussian filter, $\rho = 0.88$; (*c*) cut-off filter, $\rho = 0.42$; (*d*) $\hat{\varphi}_\ell(\boldsymbol{k}) = \exp[-(k/k_c)^8]$ filter, $\rho = 0.62$.

the filter scale $k_c = 32$ is already sufficiently far from the dissipation range and the correlation coefficient remains nearly the same as for the other larger-scale filters.

So far we have demonstrated the high level of correlations between the traceless tensors $\mathscr{T}_{ij}^{(T)}$ and τ_{ij}. Generally speaking, this result is sufficient to assert that these two tensors are statistically equivalent. Indeed, the traces of these tensors can be absorbed into a redefinition of the pressure. Nevertheless we will demonstrate that traces of the actual SGS stress $\mathscr{K}_\ell$ (3.3) and its tensor eddy viscosity representation $\mathscr{T}_\ell^{(T)}$ (3.4) are also strongly correlated. In figure 5 we plot the measured joint PDF of the traces of the actual SGS stress and the tensor eddy viscosity representation $\mathscr{P}(\mathscr{T}_\ell^{(T)}, \mathscr{K}_\ell)$. Here 128^3 numerical resolution is used (the data for 256^3 numerical resolution giving similar results). As may be seen from figure 5, $\mathscr{T}_\ell^{(T)}$ and $\mathscr{K}_\ell$ are strongly correlated with a correlation coefficient ρ at nearly the same level as for the other components of these tensors.

3.3. *Influence of filter type*

As noted above, a top-hat filter is positive and localized in physical space. On the other hand, this filter is oscillatory and slowly decaying in Fourier space. The cut-off filter

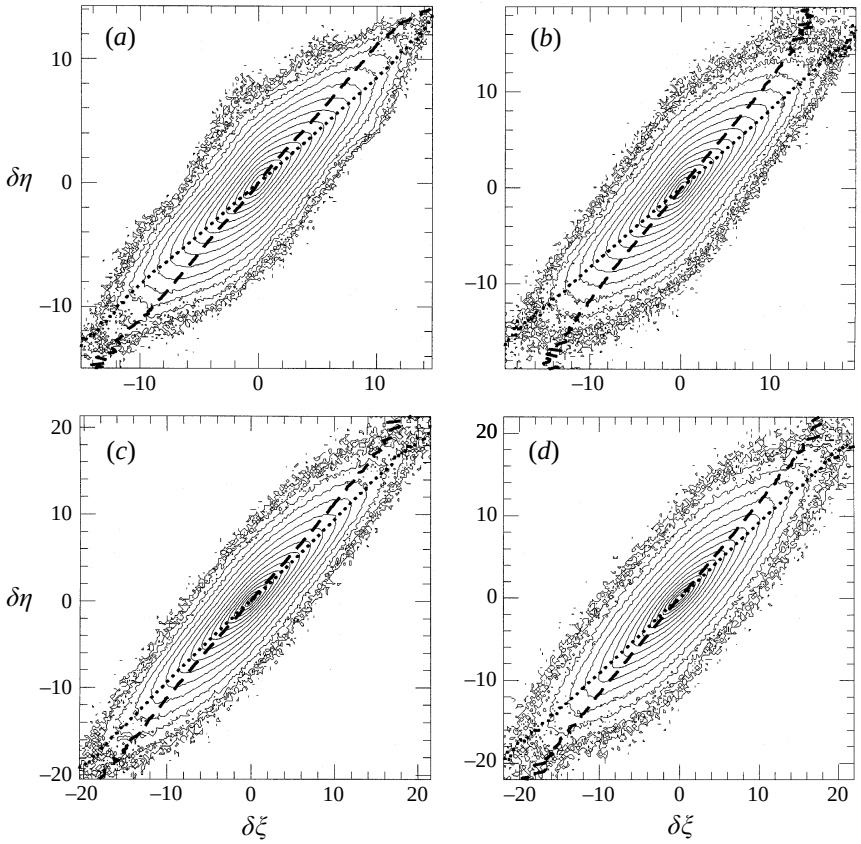

FIGURE 7. Joint PDFs between components of $\xi = N_i^{(T)}$ and $\eta = N_i^{(\tau)}$ using Gaussian filters. For details see figure 2 caption. The results are plotted for 128^3 numerical resolution ($k_d = 41$). The filter scales are (*a*) $k_c = 4$, $\rho = 0.83$; (*b*) $k_c = 8$, $\rho = 0.81$; (*c*) $k_c = 16$, $\rho = 0.89$; (*d*) $k_c = 32$, $\rho = 0.89$.

on the contrary is positive and localized in Fourier space but oscillatory and slowly decaying in physical space. Only the Gaussian filter is positive and non-oscillatory in both spaces. It is natural to use one or the other type of filter depending on what we want to stress. If we believe that the system under study behaves locally in space, the top-hat filter is a good candidate. For systems that are non-local in space but local in Fourier space, the use of the cut-off filter is more natural. In both cases, it is safe to use a Gaussian filter. In the case of fluid turbulence we prefer to use positive filters (Gaussian and top-hat) since we believe that there is substantial locality of the effective dynamical equations.

To illustrate how different filters affect the joint probability distribution $\mathscr{P}(\mathscr{T}_{ij}^{(T)}, \tau_{ij})$, in figure 6 we plot $\mathscr{P}$ for top-hat, Gaussian and cut-off filters (see (2.10)). We also presents results for a smoothed version of the cut-off filter with the Fourier transform of the filter function chosen to be $\hat{\varphi}_\ell(\boldsymbol{k}) = \exp[-(k/k_c)^8]$ with k_c defined in (2.11). The PDFs are measured for non-diagonal $i \neq j$ components of the tensors with the filter scale $k_c = 8$ (where 128^3 numerical resolution is used). As can be seen from figure 6, the correlation coefficient decreases with the decreasing filter localization in physical space. Therefore, spatially localized filters are more appropriate than non-localized ones for the representation of a spatially localized quantity such as the SGS stress tensor.

3.4. *Derivatives of the SGS stress tensor*

It is not the SGS tensor itself but rather the vector

$$N_i^{(\tau)} = \frac{\partial \tau_{ij}}{\partial x_j} \tag{3.5}$$

that participates in the filtered Navier–Stokes dynamics (see (1.2)). Therefore it is interesting to check whether the high level of correlations between τ_{ij} and its representation $\mathscr{T}_{ij}^{(T)}$ persists for the derivatives of these tensors, namely we measure the joint probability distribution between $N_i^{(\tau)}$ and

$$N_i^{(T)} = \frac{\partial \mathscr{T}_{ij}^{(T)}}{\partial x_j}. \tag{3.6}$$

The component by component joint PDF $\mathscr{P}(N_i^{(T)}, N_i^{(\tau)})$ is plotted in figure 7 for Gaussian filters and 128^3 numerical resolution.

It may be seen from figure 7 that the correlation coefficient between these two vectors remains high. We use a Gaussian filter because it is both positive and differentiable. For a top-hat filter which is not differentiable the level of correlations is slightly lower than those in the case of a Gaussian filter ($\rho \approx 0.7$).

3.5. *'Taylor expansion' and tensor eddy viscosity*

It is believed (but not yet demonstrated) that, in the limit of zero viscosity, the three-dimensional fluid velocity is not differentiable. Nevertheless, it is reasonable to assume that, in this limit, the fluid velocity is Hölder continuous (see Frisch 1995), i.e. for every point $\boldsymbol{x}$ in the flow domain the inequality

$$|\boldsymbol{v}(\boldsymbol{x}+\boldsymbol{r}) - \boldsymbol{v}(\boldsymbol{x})| \leqslant C|\mathbf{r}|^h \tag{3.7}$$

is satisfied for some C that may depend on x. Moreover, we expect that the fluid velocity field is continuous, i.e. $h > 0$. In the Kolmogorov theory of turbulence $h = 1/3$ in the inertial range. For continuous but non-differentiable velocity, we expect that in the neighbourhood of a point $\boldsymbol{x}$, a 'fractal' Taylor expansion

$$v_i(\boldsymbol{x}+\boldsymbol{r}) = v_i(\boldsymbol{x}) + r^{h-1} C_{ij} r_j + \ldots \tag{3.8}$$

holds. In (3.8), the ellipsis indicates terms of higher order in r. If we apply an isotropic filter to (3.8), the second term of this expansion gives a zero contribution leading to the estimate

$$v_i(\boldsymbol{x}) \approx \langle v_i(\boldsymbol{x}) \rangle_\ell . \tag{3.9}$$

The tensor C_{ij} may be estimated in terms of the filtered velocity gradient $\langle A_{ij} \rangle_\ell$ (1.11). Indeed $\langle A_{ij} \rangle_\ell$ can be straightforwardly calculated in terms of the second term in (3.8) leading to

$$C_{ij} = \frac{3}{(h+2)\langle r^{h-1} \rangle_\ell} \langle A_{ij} \rangle_\ell , \tag{3.10}$$

where $\langle r^n \rangle_\ell$ is defined as

$$\langle r^n \rangle_\ell = \int \varphi_\ell(\boldsymbol{r}) r^n \mathrm{d}\boldsymbol{r}. \tag{3.11}$$

Using the definition of the SGS stress (1.3) and the 'Taylor expansion' (3.8), we

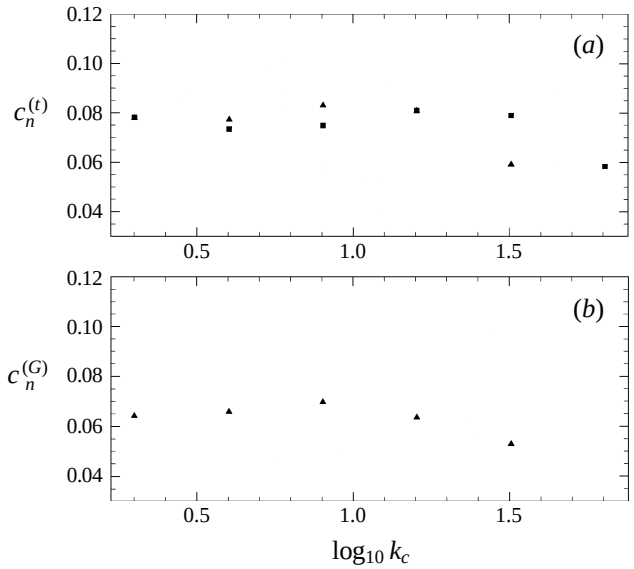

FIGURE 8. The coefficient of proportionality in the tensor eddy viscosity representation as a function of filter scale $\log_{10} k_c$. The data for numerical resolution 128^3, 256^3 are plotted as triangles, squares, respectively. (*a*) The coefficient for the top-hat filter $c_n^{(t)}$. (*b*) The coefficient for the Gaussian filter $c_n^{(G)}$.

obtain for an isotropic filter

$$\tau_{ij} = \left(\frac{3}{(h+2)\,\langle r^{h-1} \rangle_\ell} \right)^2 \frac{\langle r^{2h} \rangle_\ell}{3} \langle A_{ik} \rangle_\ell \langle A_{jk} \rangle_\ell . \tag{3.12}$$

The representation (3.12) implies that the coefficient c_n in (1.10) equals

$$c_n^{(t)} = \frac{1}{4(2h+3)} \tag{3.13}$$

for the top-hat filter and

$$c_n^{(G)} = \frac{3\pi^{1/2}\Gamma(h+3/2)}{20(h+2)^2\Gamma^2(1+h/2)} \tag{3.14}$$

for the Gaussian filter. In (3.14), Γ is the Gamma-function. With $h = 1/3$ we obtain $c_n^{(t)} \approx 0.068$ and $c_n^{(G)} \approx 0.049$.

We also measure c_n using the computed joint PDF. It is found that, independently of which component is used, the same coefficient is obtained. The data are plotted in figure 8 for the Gaussian and top-hat filters and numerical resolutions 128^3 and 256^3. These results show that the values of c_n are nearly independent of scale (except for the case of the smallest filter sizes) and of Reynolds number. The values of c_n are slightly above the predictions (3.13) and (3.14) obtained for $h = 1/3$. Considering the qualitative nature of these predictions, the actual numerical values for c_n are surprisingly close.

It is interesting to note that this Taylor expansion approach allows an easy generalization of the SGS stress representation for non-isotropic filters, which may be important for problems with non-uniform meshes. Such meshes are typical in most practical LES applications. To treat non-uniform meshes correctly, both

inhomogeneous and anisotropic filters should be used. In the case of such filters, the generalization of the tensor eddy viscosity parametrization of the SGS stress tensor takes the form

$$\tau_{ij} = J_{mn}(\ell)\,\langle A_{im}\rangle_\ell\,\langle A_{jn}\rangle_\ell\,, \tag{3.15}$$

where

$$J_{mn}(\ell) \propto \int \varphi_\ell(\boldsymbol{r}) r_m r_n \mathrm{d}\boldsymbol{r} \tag{3.16}$$

is proportional to (and indeed nearly equals) the moment of inertia of the filter.

4. Local energy flux

The local energy flux is defined from the energy balance (1.4) as

$$\boldsymbol{\Pi}_\ell = -\partial_i\,\langle v_j\rangle_\ell\,\tau_{ij}. \tag{4.1}$$

In the tensor eddy viscosity representation, the actual local energy flux may be parametrized as

$$\boldsymbol{\Pi}_\ell^{(T)} = c_n \ell^2 [-\mathrm{Tr}\left(\langle \boldsymbol{S}\rangle_\ell^3\right) + \tfrac{1}{4}\,\langle \omega_i\rangle_\ell\,\langle S_{ij}\rangle_\ell\,\langle \omega_j\rangle_\ell]. \tag{4.2}$$

The joint PDF $\mathscr{P}(-\boldsymbol{\Pi}_\ell^{(T)}, -\boldsymbol{\Pi}_\ell)$ is plotted in figure 9 using top-hat filters and 128^3 numerical resolution. It can be seen that the representation (4.2) correctly describes the behaviour of the local energy flux (4.1) with a correlation coefficient as high as for component-by-component correlation between the SGS stress and its tensor eddy viscosity representation. The local energy flux is predominately positive, leading on average to dissipation of energy. However, with a substantial probability the local energy flux may become negative leading to so-called energy backscattering. It is interesting that the level of correlations between the local energy flux and its tensor eddy viscosity representation is high both for positive and for negative values of the local energy flux.

The local energy flux may become negative due to the way it is defined. Indeed, the large-scale energy balance (1.4) shows that the local large-scale energy may change both due to the term that was called the local energy flux and due to the convective current. The convective current may lead to local increase or decrease of the energy but it cannot change the large-scale energy on the average. That is primarily the reason why we call (4.1) the local energy flux. Therefore, the subdivision between the transfer of the large-scale energy in space by the convective current and the transfer of the large-scale energy across scales by the local energy flux is not reflected by immediate local dissipation of the energy transferred to smaller scales. Indeed, this energy may return to larger scales at some other spatial point via backscatter. Also, the transfer of the energy between scales is more probable when the local energy is increasing due to convective energy transfer in space. Therefore, strictly speaking, the subdivision of energy transfer between convective transfer and local energy flux is somewhat arbitrary and illusory.

In our numerical experiments we checked that $\langle \boldsymbol{\Pi}_\ell\rangle = \bar{\varepsilon}$ with good accuracy. However, it turns out that it is impossible to predict the amount of energy that is locally dissipated knowing only the local energy flux $\boldsymbol{\Pi}_\ell$. The local dissipation at scale ℓ may be characterized as the filtered energy dissipation rate $\varepsilon_\ell = \langle \varepsilon\rangle_\ell$. The energy dissipation rate ε for flows subject to hyperviscosity is defined in (2.5). In figure 10 we plot the joint PDF $\mathscr{P}(\boldsymbol{\Pi}_\ell, \varepsilon_\ell)$; it is apparent that the level of correlation

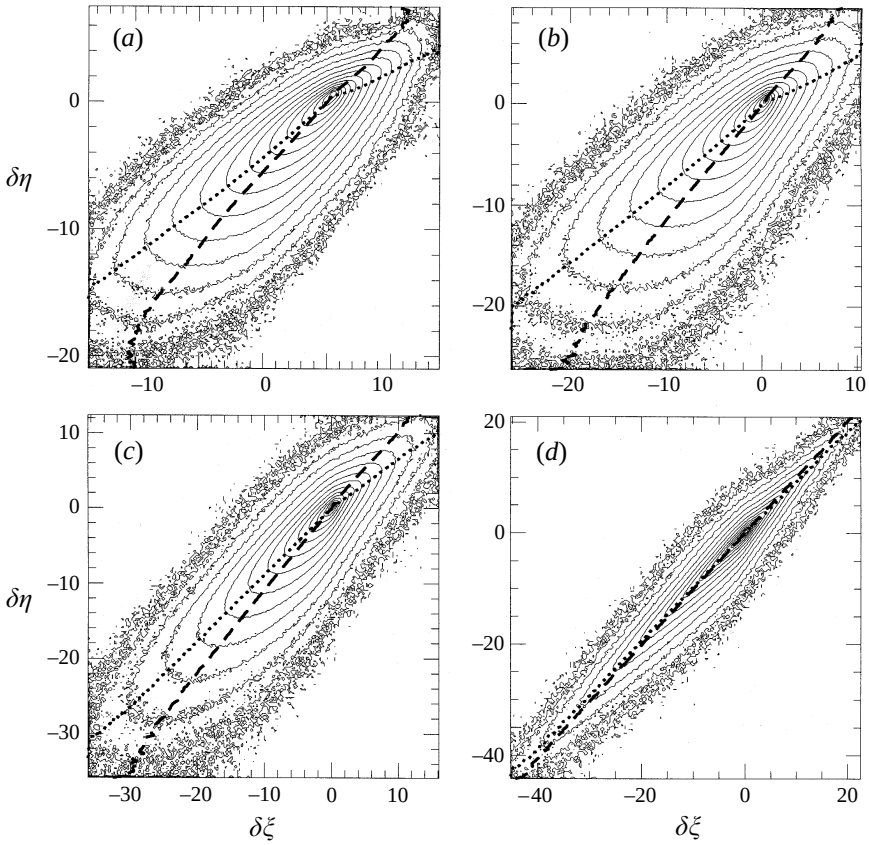

FIGURE 9. Joint PDFs between the tensor eddy viscosity representation of the local energy flux as $\xi = -\boldsymbol{\Pi}_\ell^{(T)}$ and the actual local energy flux $\eta = -\boldsymbol{\Pi}_\ell$. Top-hat filters are used. For details see figure 2 caption. The results are plotted for 128^3 numerical resolution ($k_d = 41$). The filter scales are (*a*) $k_c = 4$, $\rho = 0.87$; (*b*) $k_c = 8$, $\rho = 0.84$; (*c*) $k_c = 16$, $\rho = 0.88$; (*d*) $k_c = 32$, $\rho = 0.96$.

between the local energy flux and the local energy dissipation rate is relatively low. The conditional averages of $\langle \boldsymbol{\Pi}_\ell | \mathscr{E}_\ell \rangle$ and $\langle \mathscr{E}_\ell | \boldsymbol{\Pi}_\ell \rangle$ are both nearly linear functions of $\mathscr{E}_\ell$, $\boldsymbol{\Pi}_\ell$, respectively. That is higher $\mathscr{E}_\ell$ generally corresponds to higher local energy flux and vice versa. However, the highest values of the local energy flux do not correspond to the highest values of the local dissipation and vice versa.

The absence of strong correlations between the local energy flux and the local energy dissipation rate is not that surprising. Indeed, after energy at a certain scale ℓ is transferred to smaller scales this energy is not necessarily locally dissipated. Energy needs some time to cascade to dissipative scales. While cascading this portion of energy may be transferred back and forth in scales and convected in space, finally dissipating in another region of space. The low level of correlation between the local energy flux and the energy dissipation rate therefore reflects the cascade-like nature of the dissipation. The cascade of energy on the other hand is intimately connected with the convection of energy at inertial-range scales. The convective nature of cascades is reflected in the presence of the energy backscatter.

The local energy flux is positive if the strain matrix is negatively skewed $\mathrm{Tr}(\langle \boldsymbol{S} \rangle_\ell^3) \leqslant 0$ and/or the vorticity stretching term $\langle \omega_i \rangle_\ell \langle S_{ij} \rangle_\ell \langle \omega_j \rangle_\ell \geqslant 0$ is positive. In the next section we will show that this is indeed the case in three-dimensional homogeneous turbulence.

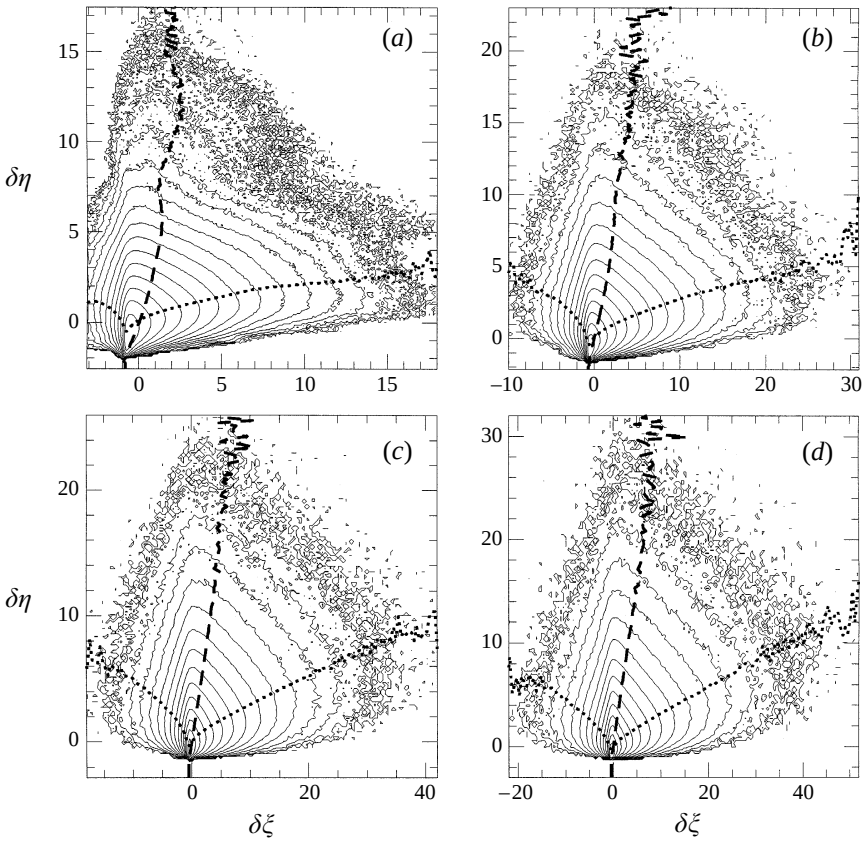

FIGURE 10. Joint PDFs between the representation of the local energy flux as $\xi = \boldsymbol{\Pi}_\ell^{(T)}$ and the local energy dissipation rate $\eta = \mathscr{E}_\ell$. Top-hat filters are used. For details see figure 2 caption. The results are plotted for 128^3 numerical resolution ($k_d = 41$). The filter scales are (*a*) $k_c = 4$, $\rho = 0.36$; (*b*) $k_c = 8$, $\rho = 0.39$; (*c*) $k_c = 16$, $\rho = 0.33$; (*d*) $k_c = 32$, $\rho = 0.31$.

5. The statistics of subgrid scales

In this section we study various statistical characteristics of the velocity gradient tensor filtered at scale ℓ.

5.1. *Dynamics of velocity gradients*

New insight into the dynamics of the local energy flux may be obtained by considering the dynamics of the filtered velocity gradients

$$\langle A_{ij}\rangle_\ell = \frac{\partial \langle v_i\rangle_\ell}{\partial x_j}. \tag{5.1}$$

The equation for the dynamics of the large-scale velocity gradient matrix takes the form

$$\frac{\mathrm{D}_\ell \langle \boldsymbol{A}\rangle_\ell}{\mathrm{d}t} + \langle \boldsymbol{A}\rangle_\ell^2 - \frac{\boldsymbol{I}}{3}\mathrm{Tr}\left(\langle \boldsymbol{A}\rangle_\ell^2\right) = \boldsymbol{H} \tag{5.2}$$

The matrix $\boldsymbol{I}$ is the unit matrix and the traceless matrix $\boldsymbol{H}$ is

$$H_{ij} = -\frac{\partial^2(p\delta_{ik} + \tau_{ik})}{\partial x_j \partial x_k} + \frac{\delta_{ij}}{3}\frac{\partial^2(p\delta_{kl} + \tau_{kl})}{\partial x_k \partial x_l}. \tag{5.3}$$

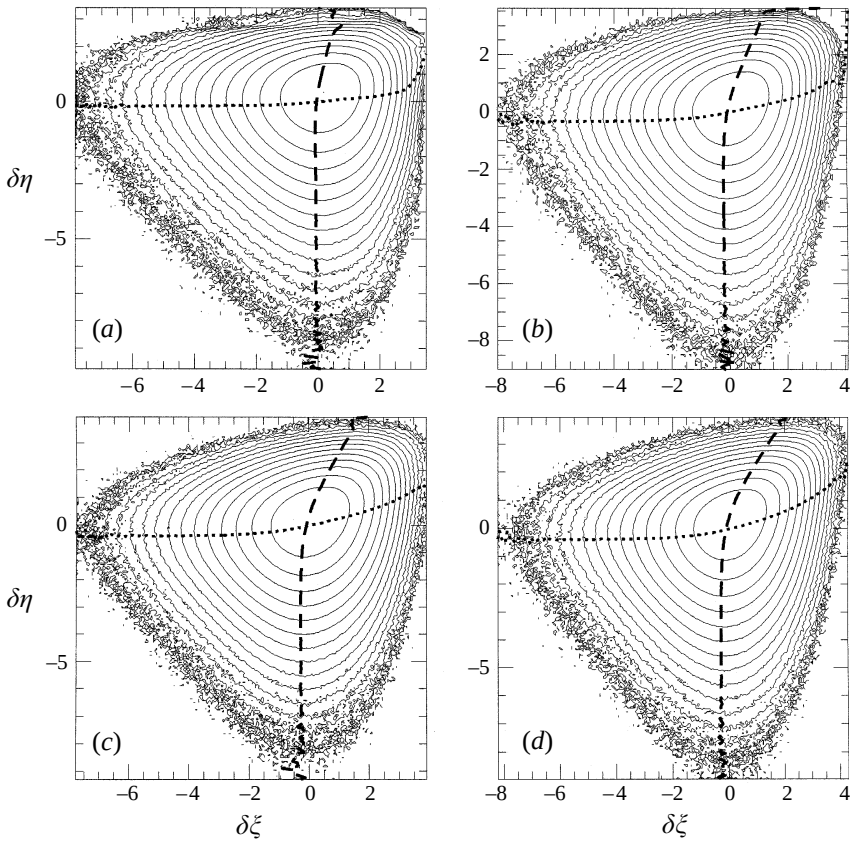

FIGURE 11. Joint PDFs between local vorticity $\xi = \ln \langle\omega\rangle_\ell^2$ and local strain $\eta = \ln \mathrm{Tr}(\langle \boldsymbol{S}\rangle_\ell^2)$. Top-hat filters are used. For details see figure 2 caption. The results are plotted for 128^3 numerical resolution ($k_d = 41$). The filter scales are (*a*) $k_c = 4$, $\rho = 0.09$; (*b*) $k_c = 8$, $\rho = 0.17$; (*c*) $k_c = 16$, $\rho = 0.21$; (*d*) $k_c = 32$, $\rho = 0.22$.

In (5.3) the matrix τ_{ij} is the SGS stress and the pressure p satisfies the equation

$$\Delta p = \tfrac{1}{2}\left\langle \omega^2 \right\rangle_\ell - \left\langle \boldsymbol{S}^2 \right\rangle_\ell . \tag{5.4}$$

The dynamics of the local energy flux is closely connected with the dynamics of local velocity gradients. We have already demonstrated that the local energy flux $\boldsymbol{\Pi}_\ell$ may be reasonably well approximated as

$$\boldsymbol{\Pi}_\ell = -c_n \ell^2 \mathrm{Tr}\left(\left\langle \boldsymbol{A}^\dagger \right\rangle_\ell \langle \boldsymbol{A} \rangle_\ell^2 \right), \tag{5.5}$$

where $\boldsymbol{A}^\dagger$ is the matrix transpose to $\boldsymbol{A}$. The SGS turbulent energy $\mathscr{K}_\ell$ in turn can be approximated as

$$\mathscr{K}_\ell = \frac{c_n \ell^2}{2} \mathrm{Tr}\left(\left\langle \boldsymbol{A}^\dagger \right\rangle_\ell \langle \boldsymbol{A} \rangle_\ell \right). \tag{5.6}$$

Then, from (5.2) the equation for $\mathscr{K}_\ell$ takes the form

$$\frac{\partial \mathscr{K}_\ell}{\partial t} = \boldsymbol{\Pi}_\ell - \frac{\partial \tilde{J}_i}{\partial x_i} + O(\ell^4), \tag{5.7}$$

where $\tilde{J}_i$ is a convective current which includes contributions from the pressure and

$O(\ell^4)$ stands for terms proportional to the SGS stress $\boldsymbol{\tau}$. Thus the energy that is transferred from the large-scales due to the local energy flux $\boldsymbol{\Pi}_\ell$ (see (1.4)) ends up as the SGS turbulent energy at low order in powers of ℓ. The SGS stress term τ_{ij} on right-hand side of (5.2) modifies this balance, introducing possible dissipation at higher order in ℓ. Therefore, although the tensor eddy viscosity representation correctly describes the dynamics of the large-scale velocity it may be not that accurate when applied to the description of filtered large-scale velocity gradients.

The matrix of filtered velocity gradients is characterized by five invariants: $\mathrm{Tr}(\langle \boldsymbol{S} \rangle_\ell^2)$, $\langle \omega \rangle_\ell^2$, $\mathrm{Tr}(\langle \boldsymbol{S} \rangle_\ell^3)$, $\langle \omega_i \rangle_\ell \langle S_{ij} \rangle_\ell \langle \omega_j \rangle_\ell$ and $(\langle S_{ij} \rangle_\ell \langle \omega_j \rangle_\ell)^2$. In this work we will study the statistical characteristics of these invariants numerically.

5.2. *Correlations between strain and vorticity*

The squares of filtered strain and vorticity are the basic quantities that characterize the level of fluctuations at a given scale. The joint probability distribution between logarithms of those quantities, $\mathscr{P}(\ln \langle \omega \rangle_\ell^2, \ln \mathrm{Tr}(\langle \boldsymbol{S} \rangle_\ell^2))$ is plotted in figure 11. The data are obtained for 128^3 numerical resolution with top-hat filters. From the results plotted in figure 11, we see that the strain and vorticity at a given scale ℓ are only weakly correlated. The correlation coefficient ρ in figure 11 measures the correlation between $\ln \mathrm{Tr}(\langle \boldsymbol{S} \rangle_\ell^2)$ and $\ln \langle \omega \rangle_\ell^2$. The correlation between $\mathrm{Tr}(\langle \boldsymbol{S} \rangle_\ell^2)$ and $\langle \omega \rangle_\ell^2$ is even weaker.

The weak correlation between strain and vorticity at a given scale is an indication of possible non-locality of Eulerian dynamics. If the dynamics are local, high vorticity will generate a high level of strain in the same region. On the other hand, strain is actually generated non-locally by high-vorticity regions across wide regions. In this latter case, the dynamics of strain is largely decoupled from the local dynamics of vorticity. Therefore, regions can exist where the flow is predominately potential or predominately vortical.

It turns out that the PDF of squares of strain and vorticity at a given scale are scale dependent. This fact is a manifestation of the well-known phenomenon of intermittency in turbulence. Unfortunately, the extent of the inertial range in our simulations does not allow us to determine the scaling exponents of these quantities reliably. Nevertheless, some important conclusions can be drawn. In figure 12 we plot PDFs of $\ln \mathrm{Tr}(\langle \boldsymbol{S} \rangle_\ell^2))$ and $\ln \langle \omega \rangle_\ell^2$ for different filter scales and different Reynolds numbers. At low strain or vorticity, these PDFs exhibit algebraic decay. Indeed, when $\xi = \mathrm{Tr}(\langle \boldsymbol{S} \rangle_\ell^2))$ is small, its PDF behaves asymptotically as $\mathscr{P} \propto \xi^{5/2}$ and, in regions of low vorticity $\eta = \langle \omega \rangle_\ell^2$, the PDF of η has the asymptotic behaviour $\mathscr{P} \propto \eta^{3/2}$.

On the other hand, for intermediate and high strains and vorticities the PDFs are approximately exponential or stretched exponentials. The PDFs fall off substantially faster than do log-normal distributions. The variance of the logarithm of strain $\ln \xi$ depends on scale approximately as $\sigma_\ell^2 \propto -0.15 \ln \ell$ and the variance of the logarithm of vorticity η behaves roughly as $\sigma_\ell^2 \propto -0.3 \ln \ell$. The averages $\langle \ln \xi \rangle$ and $\langle \ln \eta \rangle$ do not show clear scaling behaviour; rather they behave crudely as $1/\ell^{4/3}$ in accordance with Kolmogorov (1941) theory. Since the scaling of the moments of ξ^n and η^n with $n > 0$ is dominated by large strains and vorticities, the logarithmic dependence of variances may lead to scaling laws for $\langle \xi^n \rangle$ and $\langle \eta^n \rangle$ with scaling exponents that depend on n. Although we cannot determine these scaling exponents one qualitative conclusion can be drawn. The vorticity at a given scale is rather more intermittent than strain. We think that this fact reflects the presence of strong vortical coherent structures in the fluid.

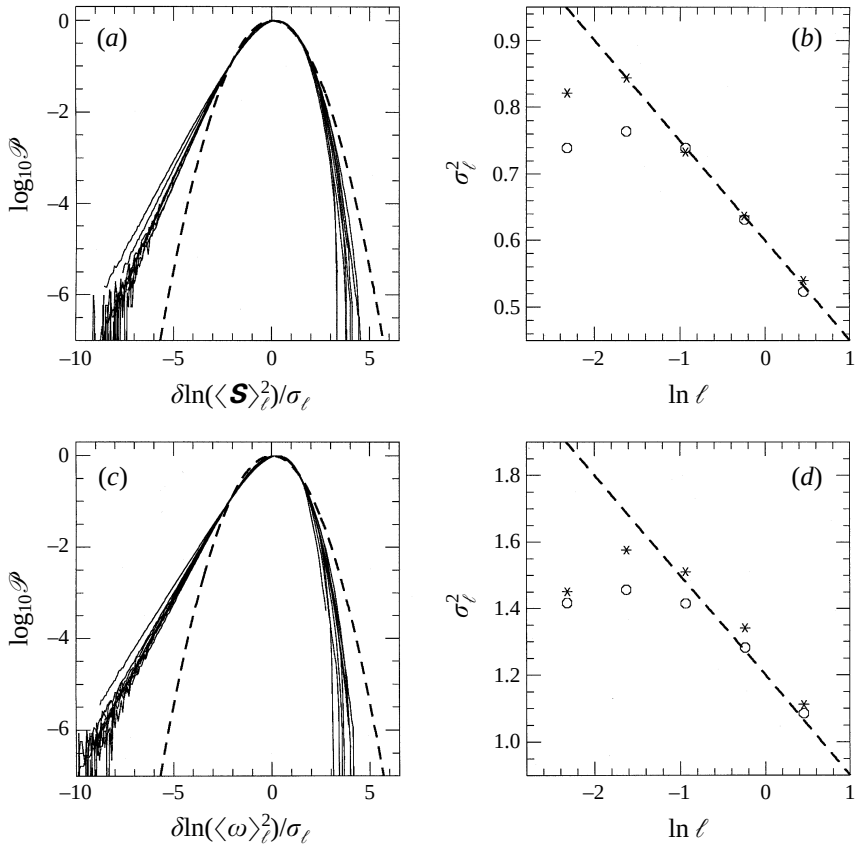

FIGURE 12. (*a*) PDFs of the local strain $\ln(\xi = \mathrm{Tr}(\langle \boldsymbol{S}\rangle_\ell^2))$. (*c*) PDF's of the local vorticity $\ln(\eta = \langle\omega\rangle_\ell^2)$. Top-hat filters are used with $k_c = 2, 4, ..., 64$. Means are subtracted and variables are normalized by their variances. Curves are superimposed for 128^3 and 256^3 numerical resolutions. Dashed curves correspond to the Gaussian PDF. The variances of local strain $\ln \mathrm{Tr}(\langle \boldsymbol{S}\rangle_\ell^2))$ and local vorticity $\ln\langle\omega\rangle_\ell^2$ are plotted as functions of scale in (*b*) and (*d*), respectively. The dashed lines in (*b*) and (*d*) correspond to interpolation formula for the variance of ξ (*b*) $\sigma_\ell^2 \propto -0.15\ln\ell$ and for the variance of η (*d*) $\sigma_\ell^2 \propto -0.3\ln\ell$.

5.3. *Negative skewness of the strain tensor*

The symmetric matrix of strain is characterized by its real eigenvalues. In the following, it will be convenient to introduce a parametrization of the eigenvalues of the large-scale strain matrix $\langle S_{ij}\rangle_\ell$. This matrix is traceless and always has real eigenvalues $z_{1,2,3}$ that satisfy the characteristic equation.

$$z^3 - \tfrac{1}{2}\mathrm{Tr}\left(\langle \boldsymbol{S}\rangle_\ell^2\right) z - \tfrac{1}{3}\mathrm{Tr}\left(\langle \boldsymbol{S}\rangle_\ell^3\right) = 0. \tag{5.8}$$

It is convenient to parametrize these eigenvalues as

$$z_i = \Gamma\cos\left(\tfrac{1}{3}\psi\right)\lambda_i \quad \text{with} \quad \Gamma = \frac{\mathrm{Tr}\left(\langle \boldsymbol{S}\rangle_\ell^2\right)^{1/2}}{\sqrt{6}} \quad \text{and} \quad \cos\psi = \frac{\mathrm{Tr}\left(\langle \boldsymbol{S}\rangle_\ell^3\right)}{6\Gamma^3}. \tag{5.9}$$

In equation (5.9) ψ varies from zero to π and the normalized eigenvalues are

$$\lambda_1 = 2; \qquad \lambda_2 = -1 + \sqrt{3}\tan\tfrac{1}{3}\psi; \qquad \lambda_3 = -1 - \sqrt{3}\tan\tfrac{1}{3}\psi. \tag{5.10}$$

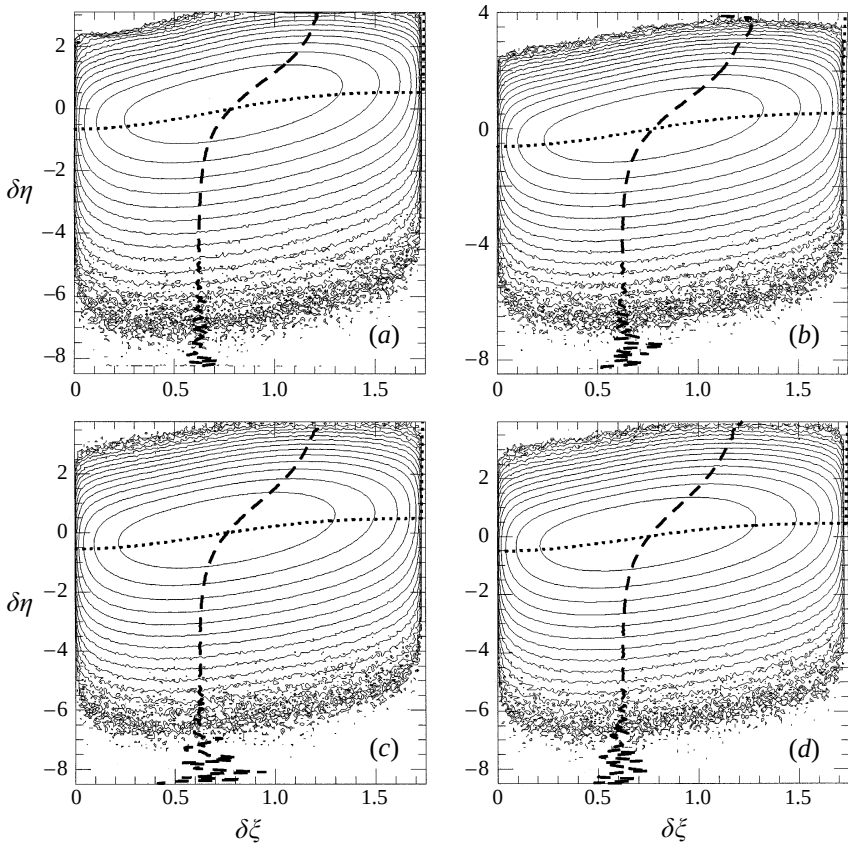

FIGURE 13. Joint PDFs between $\xi = \tan(\psi/3)$ and local strain $\eta = \ln \mathrm{Tr}(\langle \boldsymbol{S} \rangle_\ell^2)$. Top-hat filters are used. The mean of η is subtracted and η is normalized by its variance. The variable ξ is represented as raw data. The coefficient ρ is the correlation coefficient between these two fields. Isocontours of $\log_{10} \mathscr{P}$ are plotted in increments of 0.4. Dotted curves are conditional averages of abscissas conditioned on ordinates and dashed curves are vice versa. The results are plotted for 128^3 numerical resolution ($k_d = 41$). The filter scales are (*a*) $k_c = 4$, $\rho = 0.35$; (*b*) $k_c = 8$, $\rho = 0.33$; (*c*) $k_c = 16$, $\rho = 0.3$; (*d*) $k_c = 32$, $\rho = 0.28$.

It follows from (5.9) and (5.10) that the matrix $\langle \boldsymbol{S} \rangle_\ell$ is negatively skewed, $\mathrm{Tr}(\langle \boldsymbol{S} \rangle_\ell^3) \leqslant 0$, when $\psi > \pi/2$. In this case the middle eigenvalue $\lambda_2 \geqslant 0$.

The direction of the local energy flux represented using the resolved velocity gradient (1.11) is largely determined by the skewness of the strain matrix which is characterized by $\cos\psi$. If $\cos\psi < 0$, the strain matrix is negatively skewed and the local energy flux tends to be positive. Since the eigenvalues are labelled so that $\lambda_1 > 0$ and $\lambda_3 < 0$, negative skewness of the strain tensor translates into a positive middle eigenvalue $\lambda_2 \geqslant 0$. The skewness is negative when $\tan\psi/3 \geqslant 1/\sqrt{3}$. The phenomenological foundations for negative skewness of the strain tensor are extensively discussed in Monin & Yaglom (1975) together with early experimental results. Numerically, negative skewness was analysed by Ashurst *et al.* (1987) for the unfiltered strain tensor. In this work we will study the skewness of the filtered strain tensor and its dependence on the filter scale ℓ.

The joint PDF of $\mathscr{P}(\tan(\psi/3), \ln \mathrm{Tr}(\langle \boldsymbol{S} \rangle_\ell^2))$ is plotted in figure 13. The data are obtained for top-hat filters and 128^3 numerical resolution (the data for the 256^3

numerical resolution being quite similar). Based on this distribution it is possible to calculate various characteristics of the eigenvalues of the strain matrix. It can be seen from figure 13 that the conditionally averaged $\tan(\psi/3)$ changes from roughly $1/\sqrt{3}$ in low-strain regions to roughly $2/\sqrt{3}$ in high-strain regions. If we need to know the conditionally averaged eigenvalues, the averaging should be performed for the expressions (5.9). It turns out that the difference between conditionally averaged eigenvalues and eigenvalues obtained by (5.10) with conditionally averaged $\tan(\psi/3)$ is quite small. Therefore, the eigenvalues (z_1, z_2, z_3) are proportional to $(1, 0, -1)$ in the case of low strain. In the case of the high strain, the proportionality is $(1, 0.5, -1.5)$. The average proportionality of the eigenvalues is $(1, 0.15, -1.15)$. This should be compared to $(1, 0.33, -1.33)$ observed by Ashurst *et al.* (1987). We attribute this difference to the fact that we use the filtered strain matrix and the Reynolds number in our simulations is significantly higher. The average skewness $\cos\psi \approx -0.3$. This value is in general accord with the velocity difference skewness observed in our numerical simulations. It is important that the dynamics of the strain skewness is self-similar. The ratios of eigenvalues as well as the skewness $\cos\psi$ are nearly independent of scale and Reynolds number.

As can be seen from figure 13, the level of correlations ρ between $\tan(\psi/3)$ and $\ln \mathrm{Tr}(\langle \boldsymbol{S} \rangle_\ell^2)$ is not high. Also the PDFs of $\tan(\psi/3)$ for fixed $\ln \mathrm{Tr}(\langle \boldsymbol{S} \rangle_\ell^2)$ is rather broad. Therefore, the negative skewness of the filtered strain matrix should be considered as a distinct tendency but it should not be used to predict the value of $\mathrm{Tr}(\langle \boldsymbol{S} \rangle_\ell^3)$ based on the value of $\mathrm{Tr}(\langle \boldsymbol{S} \rangle_\ell^2)$. On the other hand, if we directly calculate the correlation coefficient between $\mathrm{Tr}(\langle \boldsymbol{S} \rangle_\ell^2)$ and $\mathrm{Tr}(\langle \boldsymbol{S} \rangle_\ell^3)$ we will get $\rho \approx 0.77 - 0.85$. So a relatively weak correlation between ratios of two quantities does not necessarily translate into a weak correlation between these quantities.

We also measured the joint PDF of $\mathscr{P}(\tan(\psi/3), \ln \langle \omega \rangle_\ell^2)$. It turns out that the eigenvalues of the strain matrix are nearly independent of the filtered vorticity. This is in good agreement with the generally low level of correlations between the squares of filtered strain and vorticity.

5.4. *Alignment of vorticity with the matrix of strain*

We are also interested in the dynamics of the vorticity stretching term $\langle \omega_i \rangle_\ell \langle S_{ij} \rangle_\ell \langle \omega_j \rangle_\ell$. We characterize the alignment between the vorticity vector $\langle \omega_i \rangle_\ell$ and the vector $\langle S_{ij} \rangle_\ell \langle \omega_j \rangle_\ell$ by the angle φ defined as

$$\cos\varphi = \frac{\langle \omega_i \rangle_\ell \langle S_{ij} \rangle_\ell \langle \omega_j \rangle_\ell}{\left[\left(\langle S_{ij} \rangle_\ell \langle \omega_j \rangle_\ell \right)^2 \langle \omega_i \rangle_\ell^2 \right]^{1/2}}. \tag{5.11}$$

This angle characterizes the general alignment between strain and vorticity. If $\cos\varphi \geqslant 0$, the vorticity vector is aligned with one of the positive eigenvalues of the strain. Although this angle does not give precise information with respect to which eigenvector the vorticity is aligned with, it is useful to characterize the positivity of the vorticity stretching term.

The joint PDF $\mathscr{P}(\cos\varphi, \ln \mathrm{Tr}(\langle \boldsymbol{S} \rangle_\ell^2))$ is plotted in figure 14. When the strain is low the conditionally average $\cos\varphi$ is equal to zero. At higher levels of strain, $\cos\varphi > 0$ and the vorticity stretching term $\langle \omega_i \rangle_\ell \langle S_{ij} \rangle_\ell \langle \omega_j \rangle_\ell$ is therefore positive. It is interesting that this joint PDF is nearly independent of the scale ℓ at which it is measured. The behaviour of the conditionally averaged $\cos\varphi$ is similar to the behaviour of the conditionally averaged $\tan(\psi/3)$ discussed above. We also measured the joint

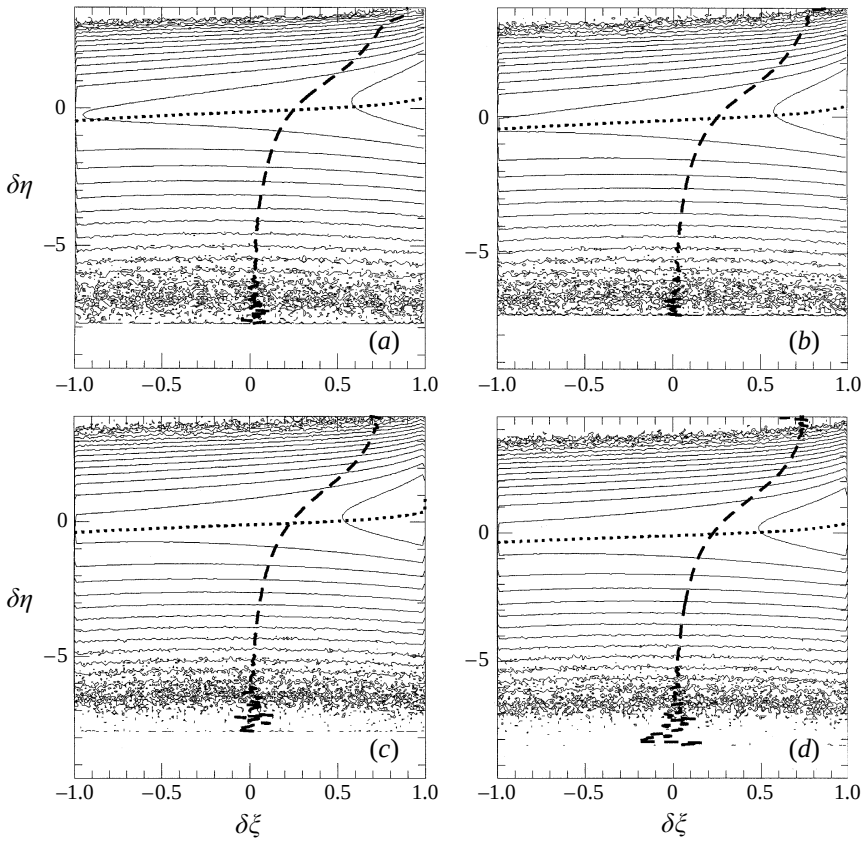

FIGURE 14. Joint PDFs between $\xi = \cos\varphi$ and local strain $\eta = \ln \mathrm{Tr}(\langle \boldsymbol{S} \rangle_\ell^2)$. Top-hat filters are used. For details see figure 13 caption. The filter scales are (*a*) $k_c = 4$, $\rho = 0.22$; (*b*) $k_c = 8$, $\rho = 0.22$; (*c*) $k_c = 16$, $\rho = 0.2$; (*d*) $k_c = 32$, $\rho = 0.19$.

PDF $\mathscr{P}(\cos\varphi, \langle\omega\rangle_\ell^2)$. In contrast with the case of strain, $\cos\varphi$ and $\langle\omega\rangle_\ell^2$) are nearly independent.

To be more specific, it is convenient to parametrize the normalized vorticity vector by the projections of this vector on the eigenvectors of the strain. We define the squares of these projections as Ω_i^2 with i meaning the projection on the ith eigenvector. By definition $\Omega_i \Omega_i = 1$. It is possible to express Ω_i through the invariants of the velocity gradient matrix. For example

$$\Omega_1^2 = \frac{z_1 \langle\omega_i\rangle_\ell \langle S_{ij}\rangle_\ell \langle\omega_j\rangle_\ell + \left(\langle S_{ij}\rangle_\ell \langle\omega_j\rangle_\ell\right)^2 + z_2 z_3}{(z_1 - z_3)(z_1 - z_2)\langle\omega_i\rangle_\ell^2} \tag{5.12}$$

with other Ω_i obtained by cyclic permutations of the indexes $(1, 2, 3)$.

As an example of alignment of the filtered vorticity vector with the filtered strain, we plot in figure 15 the joint PDFs $\mathscr{P}(\Omega_2, \ln \mathrm{Tr}(\langle \boldsymbol{S} \rangle_\ell^2))$ and $\mathscr{P}(\Omega_1, \ln \mathrm{Tr}(\langle \boldsymbol{S} \rangle_\ell^2))$ for top-hat filters with filter scales $k_c = 4$ and $k_c = 16$. The behaviour of this alignment is also nearly scale independent. As may be seen from figure 15, Ω_1 is nearly independent of strain (and is nearly independent of local vorticity as well). We find the averages $\langle\Omega_1\rangle = 0.5$ and $\langle\Omega_1^2\rangle = 1/3$. In contrast, the projection on the middle eigenvector depends on the level of filtered strain (and is nearly independent of filtered vorticity). The conditional Ω_2 changes from $1/2$ for low strain to roughly 0.75-0.8 when the

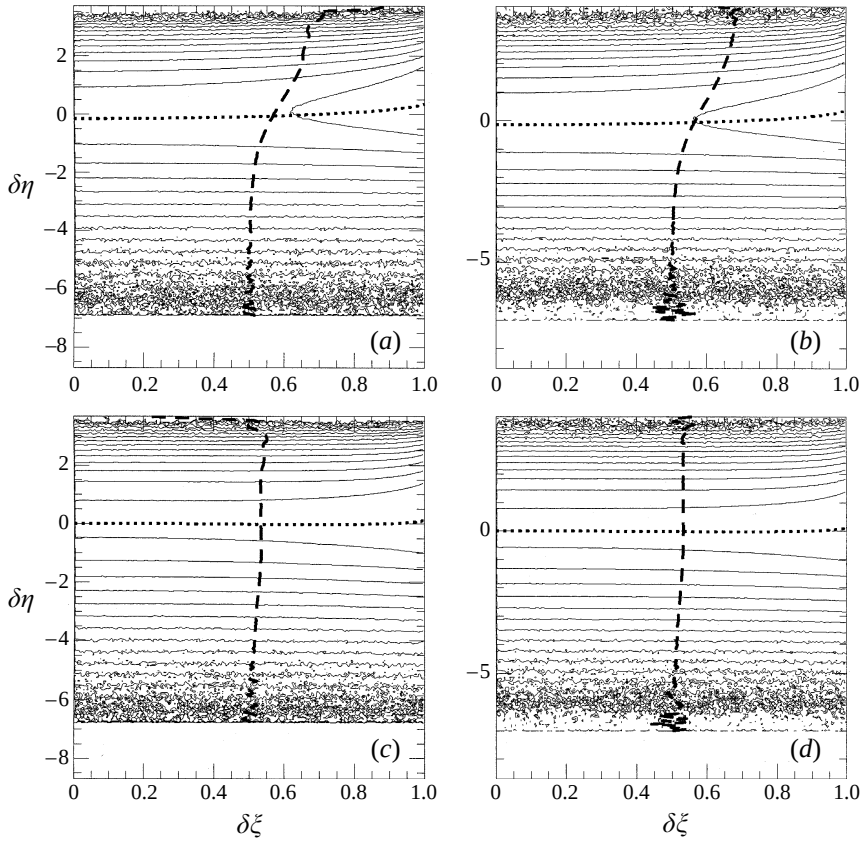

FIGURE 15. Joint PDFs between $\xi = \Omega_i$ and local strain $\eta = \ln \mathrm{Tr}(\langle \boldsymbol{S} \rangle_\ell^2)$. Top-hat filters are used. For details see figure 13 caption. The results are plotted for 128^3 numerical resolution ($k_d = 41$). The filter scales are (*a*) $k_c = 4$, $\xi = \Omega_2$, $\rho = 0.13$; (*b*) $k_c = 16$, $\xi = \Omega_2$, $\rho = 0.12$; (*c*) $k_c = 4$, $\xi = \Omega_1$, $\rho = 0.003$; (*d*) $k_c = 32$, $\xi = \Omega_1$, $\rho = 0.005$.

strain is high. These results are in accord with the data of Ashurst *et al.* (1987) except of the fact that in our case no correlation between Ω_1 and strain is observed. In contrast, Ashurst *et al.* (1987) find some decrease of Ω_1 at high levels of local strain.

5.5. *Restricted Euler dynamics*

It was noticed by Viellefosse (1982) that if the matrix $\boldsymbol{H}$ (5.3) can be neglected the remaining equation is closed. Equation (5.2) with the term $\boldsymbol{H}$ neglected is called the restricted Euler equation. It was shown by Viellefosse (1982, 1984) that restricted Euler dynamics lead to the formation of a singularity in finite time. The exact solution of the restricted Euler equations was obtained by Cantwell (1992). It is not yet known whether this singularity is an unphysical prediction of restricted Euler dynamics (but R. Pelz 1996 and R. Kerr 1996, personal communications, argue forcibly that singularities persist in the Euler dynamics at least for special initial conditions). We note that when the singularity of (5.2) tends to form, the assumptions leading to the restricted Euler equation become no longer valid. Nevertheless the restricted Euler equation predicts strong negative skewness of $\mathrm{Tr}(\langle \boldsymbol{S} \rangle_\ell^3)$, i.e. the middle eigenvalue of the strain matrix tends to be positive. Another prediction is the tendency of $\langle \omega_i \rangle_\ell \langle S_{ij} \rangle_\ell \langle \omega_j \rangle_\ell$

to become positive. More accurately, the restricted Euler dynamics predicts that the vorticity vector tends to align with the eigenvector of strain corresponding to the middle eigenvalue of strain. This type of behaviour is also observed in our simulations, although the observed alignment is not as strong as predicted by the restricted Euler dynamics.

Following Cantwell (1992) it is convenient to define the invariants

$$Q = -\tfrac{1}{2}\mathrm{Tr}\left(\langle \boldsymbol{A}\rangle_\ell^2\right) = \tfrac{1}{4}\langle\omega\rangle_\ell^2 - \tfrac{1}{2}\langle \boldsymbol{S}\rangle_\ell^2 \tag{5.13}$$

and

$$R = -\tfrac{1}{3}\mathrm{Tr}\left(\langle \boldsymbol{A}\rangle_\ell^3\right) = -\tfrac{1}{3}\mathrm{Tr}\left(\langle \boldsymbol{S}\rangle_\ell^3\right) - \tfrac{1}{4}\langle\omega_i\rangle_\ell \langle S_{ij}\rangle_\ell \langle\omega_j\rangle_\ell . \tag{5.14}$$

Under restricted Euler dynamics, the following quantity is conserved:

$$\tfrac{27}{4}R^2 + Q^3 = Q_0^3 = \text{const.} \tag{5.15}$$

Also the system tends to evolve to an asymptotic state with $R \to \infty$, $Q \to -\infty$ and the initial Q_0 therefore may be neglected. When the system approaches the asymptotic state, equation (5.15) is satisfied with $Q_0 \approx 0$.

Note that the level of correlation between filtered strain and vorticity that we report is rather low. The decoupling between strain and vorticity is in contradiction with restricted Euler dynamics, in which high vorticity is always accompanied by high levels of strain and vice versa. In particular, singular behaviour of strain and vorticity takes place simultaneously.

It is interesting to compare the definition of R in (5.14) with the expression for the local energy flux (1.12). Both these expressions contain similar terms with different weights. As already discussed, the term $\mathrm{Tr}(\langle \boldsymbol{S}\rangle_\ell^3)$ has a tendency to become negative at high levels of strain. The vorticity stretching term $\langle\omega_i\rangle_\ell \langle S_{ij}\rangle_\ell \langle\omega_j\rangle_\ell$ by contrast tends to become positive when the level of strain is high. Therefore both these terms lead to positive local energy flux $\boldsymbol{\Pi}_\ell$. By contrast, a negative skewness of strain leads to positive values of R but a positive vorticity stretching term decreases R. In view of the conservation law (5.15) within restricted Euler dynamics, it is interesting to measure the joint PDFs of Q and R as well as the joint PDFs of Q and $\boldsymbol{\Pi}_\ell$.

The joint PDFs of $\mathscr{P}(R,Q)$ and $\mathscr{P}(\boldsymbol{\Pi}_\ell,Q)$ are plotted in figure 16. We plot only the PDFs for 128^3 numerical resolution and top-hat filters with scale $k_c = 4, 16$. The PDFs for different positive filters, different filter scales and different numerical resolutions are similar.

The conservation law (5.15) of restricted Euler dynamics may be interpreted as showing that the joint PDF of $\mathscr{P}(R,Q)$ depends only on Q_0. The isolines $Q_0 = \text{const}$ and expected contour lines of the joint PDF were studied by Cantwell (1992). It is remarkable that the observed isolines of $\mathscr{P}(R,Q)$ are in close correspondence with the predictions of Cantwell (1992). In particular the conditional average $\langle R|Q\rangle$ in the region where $Q \leqslant 0$ corresponds nearly exactly to the conservation law (5.15) isoline with $Q_0 = 0$.

The isocontours of the joint PDF of the local energy flux $\mathscr{P}(\boldsymbol{\Pi}_\ell,Q)$ are noticeably different from those of $\mathscr{P}(R,Q)$. The local energy flux is positive in regions where strain dominates vorticity $Q \leqslant 0$. In regions where $Q \geqslant 0$, the conditional $\boldsymbol{\Pi}_\ell$ is only marginally positive. Therefore, most energy transfer by the local energy flux mechanism takes place in regions of high strain. In contrast, backscatter or negative local energy flux is predominately observed in regions dominated by vorticity.

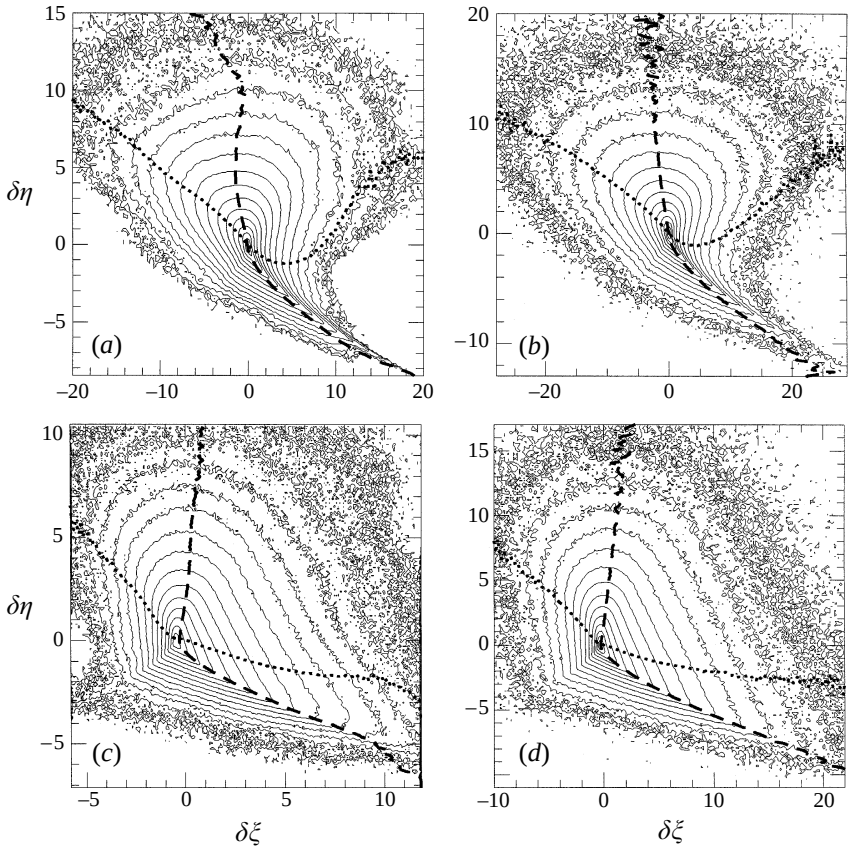

FIGURE 16. Joint PDFs $\mathscr{P}$ between $\xi = R$ and $\eta = Q$ (a, b). Joint PDFs between $\xi = \boldsymbol{\Pi}_\ell$ and $\eta = Q$ (c, d). Top-hat filters are used. For details see figure 2 caption. The filter scales are (a) $k_c = 4$, $\xi = R$, $\eta = Q$, $\rho = -0.47$; (b) $k_c = 16$, $\xi = R$, $\eta = Q$, $\rho = -0.41$; (c) $k_c = 4$, $\xi = \boldsymbol{\Pi}_\ell$, $\eta = Q$, $\rho = -0.31$; (d) $k_c = 16$, $\xi = \boldsymbol{\Pi}_\ell$, $\eta = Q$, $\rho = -0.28$.

The fact that the restricted Euler dynamics predicts the qualitatively correct form of the joint PDF $\mathscr{P}(R, Q)$ is rather surprising since other predictions such as a high level of correlation between local strain and local vorticity does not hold. In this work we test the basic assumption of restricted Euler dynamics directly, namely the possibility of neglecting the traceless matrix $\boldsymbol{H}$ (see (5.3)) in the local gradient dynamical equation (5.2).

The dynamical equations for Q and R can be obtained from (5.2), (5.13) and (5.14). The equation for Q is

$$\frac{\mathrm{D}_\ell Q}{\mathrm{d}t} + 3R + \mathrm{Tr}(\langle \boldsymbol{A} \rangle_\ell \boldsymbol{H}) = 0 \tag{5.16}$$

while the equation for R is

$$\frac{\mathrm{D}_\ell R}{\mathrm{d}t} - \tfrac{2}{3}Q^2 + \mathrm{Tr}(\langle \boldsymbol{A} \rangle_\ell \langle \boldsymbol{A} \rangle_\ell \boldsymbol{H}) = 0. \tag{5.17}$$

It is possible to neglect the matrix $\boldsymbol{H}$ only if typically $\xi_1 \gg \eta_1$ and $\xi_2 \gg \eta_2$, where $\xi_1 = 3R$, $\eta_1 = \mathrm{Tr}(\langle \boldsymbol{A} \rangle_\ell \boldsymbol{H})$, $\xi_2 = 2Q^2/3$ and $\eta_2 = -\mathrm{Tr}(\langle \boldsymbol{A} \rangle_\ell \langle \boldsymbol{A} \rangle_\ell \boldsymbol{H})$.

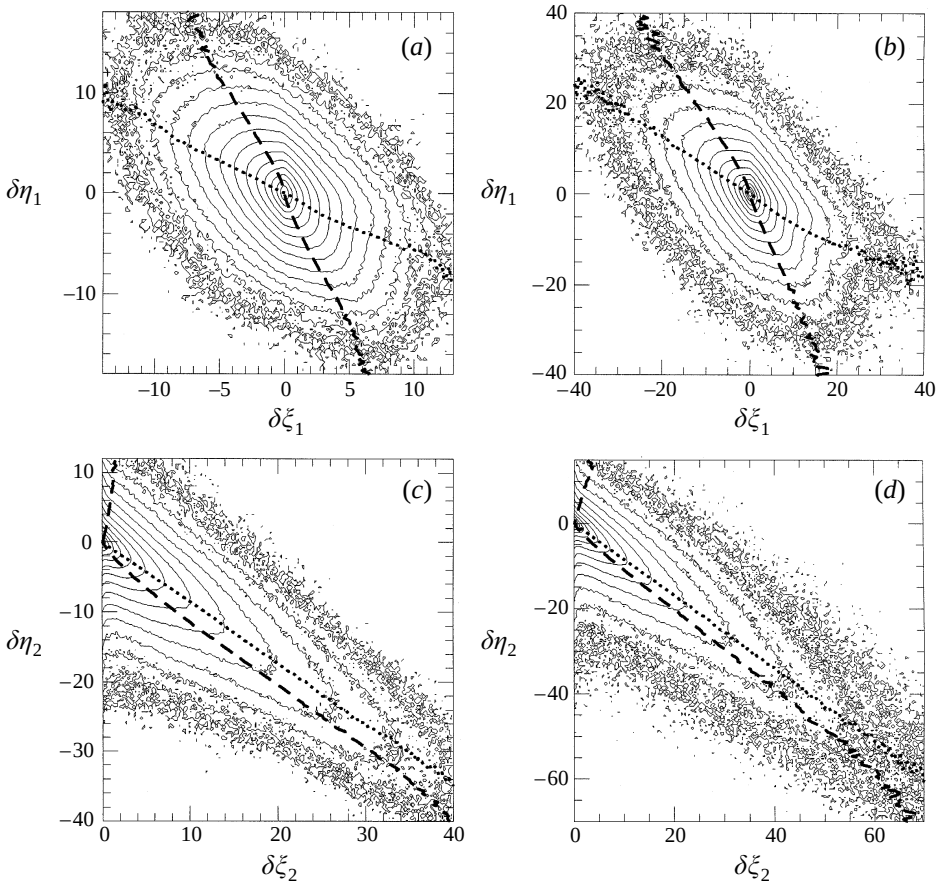

FIGURE 17. Joint PDFs $\mathscr{P}$ between $\xi_1 = 3R$ and $\eta_1 = \mathrm{Tr}(\langle \boldsymbol{A} \rangle_\ell \boldsymbol{H})$ (a, b). Joint PDFs between $\xi_2 = 2Q^2/3$ and $\eta_2 = -\mathrm{Tr}(\langle \boldsymbol{A} \rangle_\ell \langle \boldsymbol{A} \rangle_\ell \boldsymbol{H})$ (c, d). Top-hat filters are used. The variables $\xi_1(\xi_2)$ and η_1 (η_2) are normalized by the same variance of $\xi_1(\xi_2)$. For other details see figure 2 caption. The results are plotted for 128^3 numerical resolution ($k_d = 41$). The filter scales are (a) $k_c = 4$ and $\rho = -0.44$; (b) $k_c = 16$ and $\rho = -0.47$; (c) $k_c = 4$ and $\rho = -0.73$; (d) $k_c = 16$ and $\rho = -0.82$.

In figure 17, we plot the isocontours of the joint PDFs $\mathscr{P}(\xi_1, \eta_1)$ and $\mathscr{P}(\xi_2, \eta_2)$ obtained using 128^3 numerical resolution and top-hat filters with $k_c = 4, 16$ (data for other filter sizes are similar). The data in figure 17 are plotted with $\xi_1(\xi_2)$ and $\eta_1(\eta_2)$ normalized by the same variances of $\xi_1(\xi_2)$, respectively. As may be seen from figure 17, the variables ξ_1 and η_1 are negatively correlated and the variables ξ_2 and η_2 are strongly negatively correlated. Moreover, the magnitudes of the variables ξ_1 and η_1 as well as ξ_2 and η_2 are nearly equal. Therefore, it is impossible to neglect the matrix $\boldsymbol{H}$ in equation (5.2). We can make an even stronger statement that the term η_1 substantially reduces the corresponding ξ_1 term in equation (5.16). The terms ξ_2 and η_2 nearly cancel each other in equation (5.17). The substantial correlation of the $\xi_1(\xi_2)$ and $\eta_1(\eta_2)$ terms suggest that

$$\boldsymbol{H} \propto \langle \boldsymbol{A} \rangle_\ell^2 - \tfrac{1}{3} \boldsymbol{I} \mathrm{Tr}(\langle \boldsymbol{A} \rangle_\ell^2) \tag{5.18}$$

with the coefficient of proportionality in (5.18) close to unity. A somewhat similar statement is given by Cantwell (1993). The fact that at least some aspects of the

restricted Euler dynamics are still reproduced in our numerical simulations can probably be explained on the basis of the high level of correlation of the $\xi_1(\xi_2)$ and $\eta_1(\eta_2)$ terms. Apparently these terms coming from the matrix $\boldsymbol{H}$ do not cancel each other exactly but instead only slow down the evolution of Q and R and do not change the dynamics qualitatively.

5.6. *Filtered velocity gradients and velocity differences*

As we discussed above, velocity differences may be reasonably described through the filtered velocity gradients

$$\Delta_j^{(\ell)} v_i = v_i(n_j \ell) - v_i(0) \approx \ell \langle A_{ij} \rangle_\ell , \tag{5.19}$$

where n_j is the direction of measurement of velocity differences. Therefore, the statistics of velocity differences can be decomposed into the statistics of velocity gradient invariants and a trivial factor linked to the rotation of the vector n_j in space. In particular, longitudinal velocity differences may be represented as

$$\Delta_i^{(\ell)} v_i \approx \ell n_i \langle S_{ij} \rangle_\ell n_j. \tag{5.20}$$

Thus the statistics of longitudinal velocity differences are described by the dynamics of $\mathrm{Tr}(\langle \boldsymbol{S} \rangle_\ell^2)$ and $\mathrm{Tr}(\langle \boldsymbol{S} \rangle_\ell^3)$. A corresponding trivial part of the longitudinal velocity difference statistics comes from incorporating the rotational degrees of freedom due to the direction of measurements $\boldsymbol{n}$ in the velocity difference PDFs.

The statistics of transverse velocity differences are determined by the dynamics of all five velocity gradient invariants. A quantity that directly probes the statistics of vorticity only is the circulation

$$\Gamma_\ell = \oint \boldsymbol{v} \mathrm{d}\mathbf{r}. \tag{5.21}$$

We think that $\mathrm{Tr}(\langle \boldsymbol{S} \rangle_\ell^2)$ and $\langle \omega \rangle_\ell^2$ are mostly responsible for the scale dependence of filtered velocity gradients. The other three invariants depend on scale mostly through the latter two invariants, since their statistical properties are universal conditioned on $\mathrm{Tr}(\langle \boldsymbol{S} \rangle_\ell^2)$.

We expect that squares of the filtered strain and vorticity exhibit scaling behaviour and may also expect to see corrections to these scalings due to strain skewness and alignment of vorticity. Moreover, the intermittency of filtered vorticity is nearly twice as high as the intermittency of the filtered strain tensor. Therefore, the circulation (5.21) is expected to be more intermittent than longitudinal velocity differences. We may also expect the circulation to exhibit a scaling law different from that of the longitudinal velocity differences. This was indeed observed in recent laboratory measurements by Sreenivasan, Juneja & Suri (1995).

6. Discussion

The main conclusion of this paper is that the SGS stress tensor may be represented in the form of a tensor eddy viscosity

$$\tau_{ij} = c_n \ell^2 \frac{\partial \langle v_i \rangle_\ell}{\partial x_k} \frac{\partial \langle v_j \rangle_\ell}{\partial x_k}, \tag{6.1}$$

the form first suggested by Leonard (1974). The tensor eddy viscosity representation

leads to a transparent expression for the local energy flux

$$\boldsymbol{\Pi}_\ell = c_n \ell^2 \left[-\mathrm{Tr}\left(\langle \boldsymbol{S} \rangle_\ell^3 \right) + \tfrac{1}{4} \langle \omega_i \rangle_\ell \langle S_{ij} \rangle_\ell \langle \omega_j \rangle_\ell \right]. \tag{6.2}$$

The energy transfer over scales takes place in regions with negative skewness of the filtered strain tensor or in regions where the vorticity stretching term is positive. Thus the dynamics of the local energy flux is mainly determined by the dynamics of the five invariants of filtered velocity gradients.

We demonstrated that normalized quantities such as the skewness of the filtered strain matrix (see (5.9)) and the projection of vorticity on the strain matrix (see (5.11), (5.12)) universally depend on the normalized rate of strain. Scale dependence is mostly exhibited through the scale dependence of the $\mathrm{Tr}(\langle \boldsymbol{S} \rangle_\ell^2)$, $\langle \omega \rangle_\ell^2$ invariants. We also demonstrated that the vorticity invariant is more intermittent than the strain invariant. It was shown that when the level of the filtered strain is high the strain matrix is strongly negatively skewed and the vorticity stretching term is strongly positive. This leads to positive local energy flux from large to small scales.

The energy dissipation rate is found to be only rather weakly correlated with the local energy flux. This fact reflects the cascade nature of the local energy flux. Knowledge that energy is locally transferred on a certain scale to smaller scales does not lead to knowledge of what portion of that energy is indeed dissipated in that local region. This fact reflects the basic difficulties of LES schemes, namely the impossibility of predicting the energy dissipation rate through knowledge of velocity gradients at scales within the inertial range.

Moreover, it should be noted that the tensor eddy viscosity representation (6.1) is symmetric in respect to the change of the direction of time. Therefore, the filtered dynamics described by (1.1) is symmetric in respect to time reversal. Navier–Stokes dynamics is, on the contrary, not symmetric to the arrow of time. The time symmetry of the filtered Navier–Stokes dynamics is broken due to the non-zero average local energy flux. Indeed, the local energy flux (6.2) is symmetric to time reversion. Therefore, $\langle \boldsymbol{\Pi}_\ell \rangle \neq 0$ manifests the time non-reversibility of the original equations. The equation for the SGS stress τ_{ij} is by contrast non-symmetric in respect to the time reversion. Therefore, the representation (6.1) cannot be exact and should be supplemented by terms that break time reversibility. Although the tensor eddy viscosity representation will be the dominant term in the SGS representation, if used alone the time-reversible nature of the resulting effective equation will lead to energy build-up at small scales. Practical LES schemes may be obtained by supplementing the tensor eddy viscosity representation (6.1) either by a Smagorinsky eddy viscosity (1.9) with a small coefficient or by a hyperviscous dissipation. The resulting model is similar to the so-called mixed model of Bardina *et al.* (1980). We carried out LES simulations with such a mixed model. A stationary state of three-dimensional turbulence is reached with statistical properties close to that of hyperviscous simulation. It is unclear at the moment whether the addition of a tensor eddy viscosity to hyperviscous dissipation has an advantage in comparison with hyperviscous dissipation alone.

We are grateful to I. Staroselsky, M. Vergassola, and V. Yakhot for valuable discussions. One of us (S.A.O.) would like to acknowledge the hospitality of the Department of Mechanical and Aerospace Engineering at Boston University. The computations have been performed on the Intel Delta at Caltech and on the IBM PVS at Princeton. This work was supported by DARPA/ONR URI Contract N00014-92-J-1796.

REFERENCES

Ashurst, W. T., Kerstein, A. R., Kerr, R. M. & Gibson, C. H. 1987 Alignment of vorticity and scalar gradient with strain rate in simulated Navier-Stokes turbulence. *Phys. Fluids* **30**, 2343–2353.

Bardina, J., Ferziger, J. H. & Reynolds, W. C. 1980 Improved subgrid scale models for large eddy simulation. *AIAA Paper* 80–1357.

Borue, V. & Orszag, S. 1995*a* Forced three-dimensional homogeneous turbulence with hyperviscosity. *Europhys. Lett.* **29**, 687–692.

Borue, V. & Orszag, S. 1995*b* Self-similar decay of three-dimensional homogeneous turbulence with hyperviscosity. *Phys. Rev.* E **52**, R856–859.

Borue, V. & Orszag, S. 1996*a* Numerical study of three-dimensional Kolmogorov flow at high Reynolds numbers. *J. Fluid Mech.* **306** 293–323.

Borue, V. & Orszag, S. 1996*b* Kolmogorov's refined similarity hypothesis for hyperviscous turbulence *Phys. Rev.* E **53**, R21–24.

Cantwell, B. J. 1992 Exact solution of a restricted Euler equation for the velocity gradient tensor. *Phys. Fluids* A **4**, 782–793.

Cantwell, B. J. 1993 On the behavior of velocity gradient tensor invariants in direct numerical simulations of turbulence. *Phys. Fluids* A **5**, 2008–2013.

Clark, R. A., Ferziger, J. H. & Reynolds, W. C. 1979 Evaluation of subgrid models using an accurately simulated turbulent flow. *J. Fluid Mech.* **91**, 1–16.

Eyink, G. L. 1995 Local energy flux and the refined similarity hypothesis. *J. Statist. Phys.* **78**, 335.

Eyink, G. L. 1996 Large-eddy simulation and the "multifractal model" of turbulence" *a priori* estimates on subgrid flux and locality of energy transfer. *J. Fluid Mech.* (submitted).

Frisch, U. 1995 *Turbulence: The Legacy of A. N. Kolmogorov*. Cambridge University Press.

Germano, M. 1992 Turbulence: the filtering approach. *J. Fluid Mech.* **238**, 325–336.

Jackson, E., She, Z.-S. & Orszag, S. A. 1991 A case study in parallel computing: I. homogeneous turbulence on a hypercube. *J. Sci. Comput.* **6**, 27–45.

Kolmogorov, A. N. 1941 The local structure of turbulence in incompressible viscous fluid at high Reynolds number. *C. R. Acad. Sci. URSS* **30**, 301.

Leonard, A. 1974 Energy cascade in large-eddy simulation of turbulent flows. *Adv. Geophys.* **18**, 237.

Liu, S., Meneveau, C. & Katz, J. 1994 On the properties of similarity subgrid-scale models as deduced from measurements in a turbulent jet. *J. Fluid Mech.* **275**, 83–119.

Monin, A. S. & Yaglom, A. M. 1975 *Statistical Fluid Mechanics*, vol. 2. MIT Press.

Orszag, S. A. 1973 Lectures on the statistical theory of turbulence. In *Fluid Dynamics* (ed. R. Balian & J.-L. Peube), p. 235. Gordon and Breach.

Reynolds, W. C. 1990 The potential and limitations of direct and large eddy simulations. In *Whither Turbulence? or Turbulence at Crossroads* (ed. J. L. Lumley), p. 313. Springer.

She, Z.-S., Jackson, E. & Orszag, S. A. 1991 Structure and dynamics of homogeneous turbulence: models and simulations. *Proc. R. Soc. Lond.* A **434**, 101–124.

Smagorinsky, J. 1963 General circulation experiments with the primitive equations, i. the basic experiment. *Mon. Weath. Rev.* **91**, 99.

Sreenivasan, K. R., Juneja, A. & Suri, A. K. 1995 Scaling properties of circulation in moderate-Reynolds-number turbulent wakes. *Phys. Rev. Lett.* **75**, 433–436.

Viellefosse, P. 1982 Local interaction between vorticity and shear in a perfect incompressible fluid. *J. Phys. Paris* **43**, 837–842.

Viellefosse, P. 1984 Internal motion of a small element of fluid in an inviscid flow. *Physica* A **125**, 150–162.

Vreman, M., Geurts, B. & Kuerten, H. 1994 Realizability conditions for the turbulent stress tensor in large-eddy simulation. *J. Fluid Mech.* **278**, 351–362.